A Comparison of Fluid/Structure Coupling Methods for Reduced Structural Models

Georg Wellmer, Lars Reimer, Horst Flister, Marek Behr, and Josef Ballmann

Abstract. In this paper, the realisation and testing of spatial coupling methods for aeroelastic simulations with partitioned algorithms is presented. The investigated methods for spatial coupling—the transfer of loads and deformations between the wetted surface and the structural model—are the method of Finite Interpolation Elements and two other, newly-implemented interpolation methods. All three are suitable for reduced structural models, and the geometries of the wetted surface and the structural model do not have to coincide. The aeroelastic simulation tool employed and the theoretical background of the spatial coupling schemes are outlined. Different measures for the quality of the spatial coupling are derived and applied to test cases of increasing complexity. The influence of user-defined coupling parameters on the deformation projection is assessed. Based on these results and on practical considerations, the available coupling methods are compared and conclusions are drawn regarding their applicability.

1 Introduction

The civilian aircraft industry faces the necessity to reduce aircraft fuel consumption while increasing flight safety levels and maintaining passenger comfort. Furthermore, competition on the aircraft market forces manufacturers to accelerate design cycles and to reduce the costs of the actual development. This twofold pressure has brought about the widespread adoption of numerical prediction methods during all

Marek Behr · Georg Wellmer · Lars Reimer
Chair for Computational Analysis of Technical Systems (CATS), Center for Computational Engineering Science (CCES), RWTH Aachen University, Schinkelstraße 2, 52062 Aachen
e-mail: {wellmer,reimer,behr}@cats.rwth-aachen.de

Josef Ballmann
Lehr- und Forschungsgebiet für Mechanik (LFM), RWTH Aachen University, Schinkelstraße 2, 52062 Aachen
e-mail: ballmann@lufmech.rwth-aachen.de

B. Eisfeld et al. (Eds.): *Management & Minimisation of Uncert. & Errors*, NNFM 122, pp. 181–218.
DOI: 10.1007/978-3-642-36185-2_8

stages of the design process. Computational Fluid Dynamics (CFD) for the numerical prediction of the flow field about aircraft configurations are of special interest to the industry. These methods have matured to a point where they are not merely complementing costly wind tunnel test campaigns, but actually partially supplanting them. Simultaneously, improvements in structural analysis methods such as Computational Structural Dynamics (CSD) and in material sciences have led to lighter aircraft frames with greater inherent elasticity. Aeroelastic coupling effects now definitely have to be considered in the design process and thus also have to be captured by the numerical prediction methods, i.e. by Computational Aeroelasticity (CAE) solvers. A code package for the simulation of the interaction between aerodynamic, elastic and inertial forces has been developed at LFM/CATS over the last decade. Work was initiated at LFM within the framework of the Collaborative Research Centre 401 (SFB 401) [3, 28] and continued at CATS, in the course of the collaborative research project MUNA, amongst others.

In order for CAE to gain the same acceptance in the aerospace community as that already enjoyed by CFD, its solutions must prove to be trustworthy. Engineers require the numerical predictions design decisions are based on to have a dependable accuracy, which can be evaluated in two different manners: First of all, by comparison with experimental results the error incurred by the whole coupled algorithm can be estimated. It can then be used as a measure of confidence for numerical predictions regarding comparable configurations. Validation against steady and unsteady wind tunnel data has been carried out continuously at LFM/CATS, most recently in the project "High Reynolds Number Aero-Structural Dynamics" (HIRENASD) [4, 24]. This approach has the downside that without extensive parameter studies the cause of deviations—potentially each of the single-field

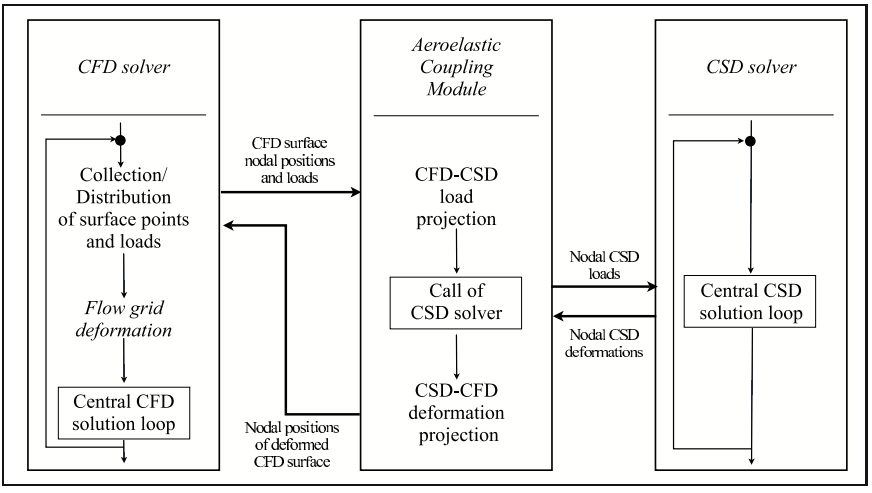

Fig. 1 General concept of the ACM and its data exchange with the CFD and CSD solvers (taken from [28])

solvers or their mutual interaction—cannot be easily determined. Besides, it must not be forgotten that also measurements inevitably have an error. In the second approach error sources are identified and examined individually, at least as far as such a separation is possible. Regarding aeroelastic coupling, it has to be demonstrated that associated sources of error do not significantly impair the accuracy of the overall coupled solution. This method often is feasible for model test cases only, and the findings have to be scrutinised before being applied to real-world problems. During the MUNA project both outlined investigation methods have been applied at LFM/CATS with regard to steady aeroelastic simulations and their associated error sources.

This paper will take the following outline: First the coupling methodology in general and the algorithm developed at LFM/CATS in particular are delineated, as well as the available spatial coupling methods. The potential error sources are defined and their influence is quantified for model problems. Next, the assessment is repeated for actual coupled flow simulations. Based on the results, the available methods for spatial coupling are compared and a set of recommendations is derived.

2 Coupling Methodology

All algorithms for the simulation of fluid-structure interaction problems fall into one of two major categories: Monolithic algorithms solve the equations governing the flow field and those governing the structural deformation simultaneously as a single set of equations [7, 21]. Partitioned algorithms employ dedicated solvers for each field which are coupled via a suitable interface. The monolithic method ensures that the mutually dependent solutions in each field are always on the same time level, which eliminates the issue of synchronising individual solvers for a conservative solution. In practise, though, this method has one significant disadvantage, which has limited its acceptance: A monolithic coupled solver generally has to be developed completely from scratch, whereas with a partitioned approach one can employ pre-existing single-field solvers and benefit from the developments of specialised research groups. Ideally, the necessary coupling interface should be sufficiently modular to allow the replacement of a single-field solver either with an updated version or with an entirely different implementation. The aeroelastic code package conceived at LFM/CATS, henceforth denoted as “Aeroelastic Coupling Module” (ACM) [9, 24, 25], is based on this rationale. The ACM allows the modular coupling of arbitrary flow and structural solvers with only minor code changes. Both steady simulations with a staggered (Block-Gauss-Seidel) algorithm and unsteady simulations with weak and strong temporal coupling schemes are possible. Pursuant to the partitioned approach followed here, the ACM serves as the interface between the dedicated single-field solvers for the flow field and for the structural deformation, as is shown in Fig. 1. The ACM carries out the synchronisation of the solvers by initiating iteratively their respective calls.

Apart from the synchronisation of the single-field solvers, the ACM also performs the spatial coupling, i.e. the projection of loads from the wetted surface to the structure and in reverse direction the projection of the structural deformations to the wetted surface. The projection methods available are tailored to reduced structural models. These are beneficial especially during unsteady simulations because of their smaller number of degrees of freedom and thus lower requirements of computational resources. With reduced structural models the geometries of the wetted surface and of the structural model coincide only in parts or not at all. This is especially true for beam models which do not even share the same dimensionality as the wetted surface. Also with more detailed models like shell models, in many cases one does not want to represent the complete structure. When modelling a wing, often only the wing box is taken into consideration. The high lift devices and other components which do not contribute significantly to the overall structural stiffness are disregarded. In both examples there are "gaps" between the wetted surface and the structural model which have to be bridged by the projection algorithm.

Because of these gaps between wetted surface and structure, forces have to be projected from the wetted surface to the structure instead of surface stresses. Latter do not possess an effective direction required in this case. As to increase the modularity of the ACM, the aerodynamic surface forces are calculated already inside the flow solver and passed on to the ACM. They should be derived in a consistent manner from the discrete distribution of surface stresses [12]. The ACM receives a cloud of load incidence points with associated force vectors and returns a cloud of surface coordinates representing the deformed wetted surface. Thus, the ACM can be coupled with structured and unstructured flow solvers alike since it is independent of the manner in which points are associated with surface cells. As a side note, the number of the load incidence points and their position in the undeformed wetted surface do not have to be identical with the surface points defining the wetted surface.

To summarise above statements, the aeroelastic coupling with the ACM comprises three steps:

1. From the pressure and surface stress distribution on the wetted surface, discrete force vectors are determined by the flow solver.
2. These surface forces are projected from the wetted surface to the nodes of the structural model.
3. The structural deformations resulting from the projected load distribution are projected back onto the wetted surface.

Each of these steps may contribute to the total error of the coupled simulation scheme. The second and third ones are closely related, though: The projection of (generalised) forces from the wetted surface to the structure can conveniently be expressed as a matrix-vector product with a force projection matrix P_F, and likewise the projection of (generalised) deformations can be expressed with a deformation projection matrix P_U:

$$\mathbf{F}_{\mathrm{CSD}} = \mathsf{P}_F \, \mathbf{F}_{\mathrm{CFD}} \quad \text{and} \quad \mathbf{u}_{\mathrm{CFD}} = \mathsf{P}_U \, \mathbf{u}_{\mathrm{CSD}} \tag{1}$$

The conservativity of the projection method is assured if $\mathsf{P}_U = \mathsf{P}_F^T$, which can be shown via the principle of virtual work [12]:

$$\begin{aligned} \delta W_{CFD} &= \mathbf{F}_{\text{CFD}}^T \, \delta \mathbf{u}_{\text{CFD}} & \delta W_{CSD} &= \mathbf{F}_{\text{CSD}}^T \, \delta \mathbf{u}_{\text{CSD}} \\ &= \mathbf{F}_{\text{CFD}}^T \, \mathsf{P}_U \, \delta \mathbf{u}_{\text{CSD}} & &= \left(\mathsf{P}_F \, \mathbf{F}_{\text{CFD}}\right)^T \delta \mathbf{u}_{\text{CSD}} \\ & & &= \mathbf{F}_{\text{CFD}}^T \, \mathsf{P}_F^T \, \delta \mathbf{u}_{\text{CSD}} \end{aligned} \tag{2}$$

Consequently, the same projection method has to be used during the projection of forces as during the projection of deformations.

A fourth step, external to the ACM, involves the deformation of the CFD volume mesh in order to accommodate the deformed wetted surface. Mesh deformation methods generally depend on the formulation of the flow solver employed, and their associated error sources are not investigated here.

2.1 Flow Solver

To date, the ACM has been coupled with three Reynolds-Averaged Navier-Stokes (RANS) Finite-Volume flow solvers: FLOWer [18, 19], TAU (recent developments are highlighted in a number of papers in this volume) and QUADFLOW [3]. In this paper, results obtained with FLOWer and with TAU are presented. The development of both solvers was initiated and led by the DLR. Further enhancement of the structured solver for multi-block topologies—FLOWer— may not be actively promoted anymore, but with that solver the greatest amount of experience has been gained in conjunction with the ACM, and the coupling can be regarded as well-validated against experiments. The effort to couple the ACM with the hybrid-unstructured solver TAU began during the previous project MEGADESIGN [20] and, for the steady branch, has been completed during MUNA. The interfaces of both flow solvers with the ACM provide the same functionality, but their implementation is quite different. FLOWer simply calls the ACM as a Fortran subroutine. The loads and load incidence points and the coordinates of the deformed wetted surface are exchanged via the subroutine parameter field. The communication between TAU and ACM used to be realised by files written on hard disk, but is now carried out completely in-memory. The solution is controlled through a script written in the object-oriented scripting language Python [26]. TAU and its components already have Python interfaces and are suitably wrapped during compilation. The ACM has to be provided as a shared object file. Specific Python interface classes contain the methods and attributes needed to perform the aeroelastic coupling. In each coupling step, the ACM's Python interface reads the loads and load incidence points from TAU's C data stream and passes them on to the ACM. In the reverse direction at the end of a coupling iteration, the interface receives the coordinates of the deformed wetted surface from the ACM and writes these to the data stream. All the while the interface has to ensure that the fields are passed on correctly between the individual software components written either in C, Fortran or Python.

For an investigation of the actual projection process it may not be relevant whether or not the loads on the wetted surface result from a flow simulation. In certain cases a user-defined load distribution may be imposed instead. This is possible with the stand-alone version of the ACM. Obviously, conclusions drawn in this manner can only regard the projection algorithm as such and not the coupled solution process as a whole.

2.2 Structural Solver

For the computation of the structural deformation, the in-house structural solver "Finite Element Analysis for Aeroelasticity" (FEAFA) is employed. It is a Finite Element (FE) code based on a physically and geometrically linearised formulation, so it is limited to small strains and linear-elastic material behaviour. Over recent years, it has been expanded to offer a range of element types comparable to commercial CSD code packages which includes volume and shell elements, spring elements, point masses and multi-freedom constraints. The mainstay for aeroelastic simulations is the multi-axial Timoshenko beam element [8, 9]. Its formulation allows for distinct cross-sectional positions of the centre of mass, the shear centre and the centre of bending. Thereby structural coupling between bending and torsional motion can be captured. The consideration of shear deformation in the Timoshenko formulations assures a physically-reasonable wave propagation through the structure, which is important for unsteady simulations. With very few degrees of freedom and thus at low computational cost, such reduced structural models are capable of accurately rendering the elastic and inertial properties of slender structures such as transport aircraft wings. This is not only a significant advantage for unsteady simulations, but also for steady design optimisation tasks, as has been demonstrated in the MEGADESIGN [20] project. During steady simulations, the structural deformation is either obtained by direct solution of the linear system of equations resulting from the FE discretisation or by superposition of pre-calculated modes.

2.3 Flow Grid Deformation

For the volume mesh deformation of structured FLOWer meshes, the Multiblock Grid Deformation Tool (MUGRIDO) [8, 16] was developed at LFM. This tool models the block boundaries of the volume mesh and selected additional mesh lines as massless Timoshenko beams. The deflections of the surface nodes relative to the undeformed configuration are imposed as boundary conditions and the structural problem is solved. Finally, the positions of the remaining mesh points inside of the blocks are calculated with transfinite interpolation. MUGRIDO is not suitable for unstructured TAU meshes. TAU offers two mesh deformation algorithms;

best suited for aeroelastic simulations with complex configurations is the weighted volume spline interpolation algorithm [15]. A further description can be found in the paper by Barnewitz in this volume. Since this method does not require any information regarding the connectivity between volume mesh points, it is equally applicable to structured meshes.

3 Spatial Coupling

The analyses presented in the paper at hand concentrate on error sources in spatial coupling, and so the description of the projection methods shall be afforded a separate section here. To begin with, an overview of projection methods suitable for reduced structural models is given. The existing projection method based on Finite Interpolation Elements (FIE) is explained. Then the newly-implemented Global Spline-Based (GSB) and Moving Least-Squares (MLS) methods are presented in detail.

In order to be valid from the physical point of view, any projection scheme has to be conservative with the following two criteria: First of all, the total force and moment vectors must be preserved during the projection. Secondly, during steady simulations the elastic strain energy of the structure must be identical to the work performed by the aerodynamic loads on the wetted surface, as implied by Eq. (2). During unsteady simulations also the instantaneous power exchanged over the coupling surface must be the same on both sides. From the flow solver and the volume mesh deformation code, further numerical requirements arise affecting the projection of deformations from the structure back to the wetted surface: The resulting deformed surface mesh should be contiguous in particular at intersections between the surface meshes of distinct assemblies, for instance between fuselage and wing. The deformed surface mesh should be smooth in order to assure good convergence of the flow solution. One final demand is of a more practical nature: With reduced structural models, any projection scheme has to make some kind of assumption for the transfer of forces and deformations over the gap between wetted surface and structure. This assumption should not be far removed from the load paths actually to be expected, i.e. some measure of locality should be preserved during the projection.

Initially, only one projection algorithm was available inside the ACM: The Finite Interpolation Element (FIE) method [5, 8, 9, 25] is an uncomplicated method that uses the shape functions of the structural model to divide aerodynamic surface loads among the nodes of the closest structural element. During the first phase of MUNA, a number of alternative projection methods was reviewed for inclusion in the ACM. Many published methods are only adequate for configurations where the wetted surface and the surface of the structural model coincide up to the discretisation error [10, 17, 22, 29]. On account of the requirements set forth for reduced

structural models such methods were excluded. Prospective methods included the Infinite-Plate Spline (IPS) method [14], the Constant-Volume-Tetrahedron (CVT) method [2, 13] and the inverse Boundary Element Method (BEM) [11]. These were extensively compared by Sadeghi et al. [27]. The GSB method [6] and the MLS method [23] constitute further alternatives suitable for reduced structural models.

With the IPS method, only the deflections normal to the wing plan form are interpolated from the structure to the wetted surface using splines as interpolation functions. This limits the method to (almost) planar configurations. With the CVT method, tetrahedra are spanned between the points on the wetted surface and the nodes of the closest structural element. Both the natural coordinates of the projection point inside the element and the volume of the tetrahedron are kept constant for all deformation states, defining the projection. As will become evident further down, the CVT method can be regarded as an extension of the FIE method. The BEM method is the projection method which is most firmly footed on physical considerations instead of geometrical neighbourhood relations: The gap between wetted surface and structure is modelled as an elastic continuum, and the deformation of the structure is expressed in terms of surface deflections through the BEM. This relation then has to be inverted with the minimisation of the elastic strain energy of the continuum as an additional constraint. Of all methods presented so far this is the most demanding. Furthermore, it requires the connectivity of the wetted surface, which currently is not transmitted from the flow solver to the ACM. The GSB and MLS methods both determine a function approximation to the nodal displacement distribution and evaluate it at the surface points. The two methods differ primarily in their choice of interpolation functions. They do not interfere with the modular structure of the ACM, offer the required generality, are independent of the dimensionality of the structural model and involve only a moderate implementation effort. Also, there is a significant implementation overlap between them, for which reason both were selected for inclusion in the ACM.

3.1 Finite Interpolation Element Method

The FIE projection method, also known as inverse isoparametric mapping, uses the shape functions of the FE structural model to interpolate loads and deformations between the points on the wetted surface and the nodes of the structural model. This results in an efficient algorithm which only requires the evaluation of algebraic expressions. The FIE method is briefly demonstrated here in conjunction with beam models. For a more elaborate description extended to structural models consisting of volume and shell elements the reader may refer to Reimer et al. [25].

The FIE method is based on purely geometrical considerations. In the first step, the closest structural element for a given point on the wetted surface is sought. Inside this element the projection point is determined. For a beam model this point

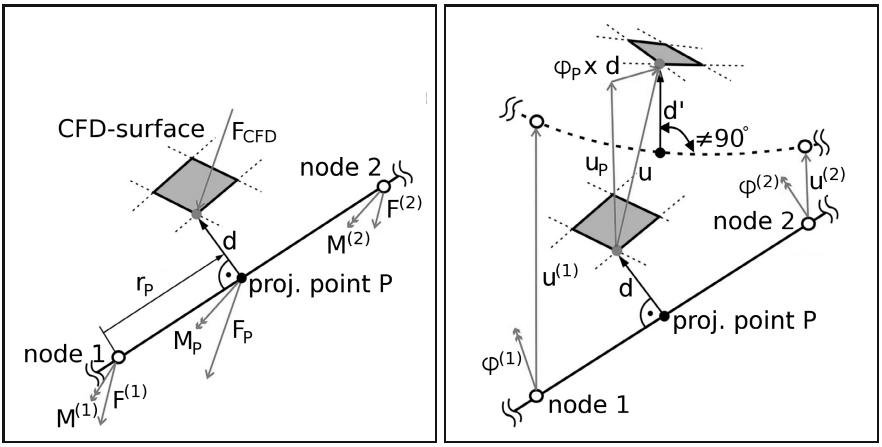

Fig. 2 Load and deformation projection with FIE on beam elements. *left:* Projection of aerodynamic forces from the wetted surface to the structure. *right:* Projection of deformations from the structure back to the wetted surface.

generally creates a perpendicular connection between surface point and beam axis, as depicted on the left of Fig. 2. The aerodynamic surface load $\mathbf{F}_{\mathrm{CFD}}$ is shifted along the distance vector $\mathbf{d}$ to the projection point $\mathbf{P}$ and an equivalent offset moment $\mathbf{M}_{\mathrm{P}} = \mathbf{d} \times \mathbf{F}_{\mathrm{CFD}}$ is introduced. With the shape functions of the element and the natural coordinate of the projection point r_{P} the force and the moment are divided among the element's nodes. The closest elements and natural coordinates of the projection points are determined only once before the first coupling step and then reused. During the deformation projection shown on the right of Fig. 2 the corresponding steps are carried out in opposite order: The rotational deformation φ_{P} and the translational deformation $\mathbf{u}_{\mathrm{P}}$ at the projection point are interpolated from the nodal values with the element shape functions. The deflection of the surface point consists of $\mathbf{u}_{\mathrm{P}}$ and a rotational contribution $\varphi_{\mathrm{P}} \times \mathbf{d}$. Even if the projection point on the undeformed beam axis created a perpendicular connection between beam axis and surface point, due to shear this may not be the case in the deformed configuration, represented by the dashed line in Fig. 2.

The methodology applied for structural models comprising shell or volume elements, which have two-dimensional projection surfaces, is the same in principle. A more involved algorithm is required to find the projection point on the closest element face. Interpolation in intersection regions has not been realised yet, so that with such structural models the FIE method in the ACM can be applied only to configurations with one assembly. The CVT method can be seen as a variant of the FIE method in which the length of the distance vector is no longer kept constant, but adapted according to the deformational change of the area of the projection face.

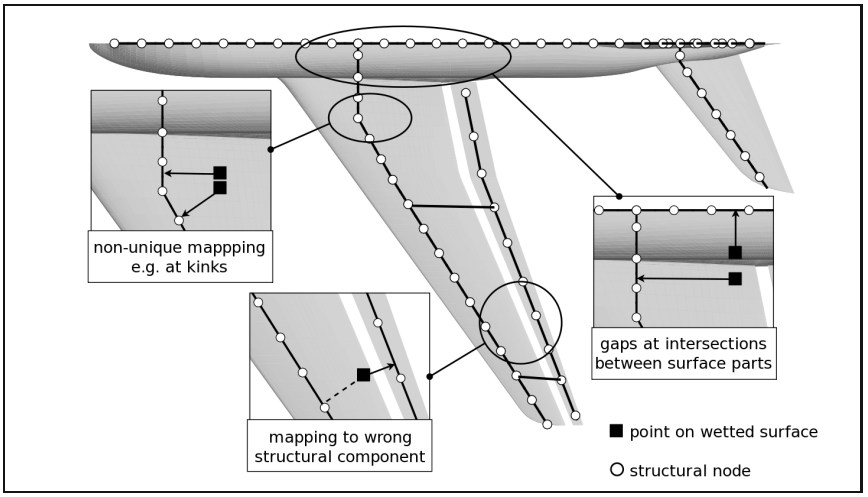

Fig. 3 Regions in which a straightforward application of the FIE method will lead to undesirable results.

3.2 Additional Interpolation Schemes for FIE

For structural models with a single straight beam axis, the FIE method is a logical extension of beam theory. The projection algorithm assures that during deformation sections through the wetted surface that were perpendicular to the beam axis in the undeformed configuration preserve their shape. If however a structure consists of several angled beam segments, possibly part of different assemblies such as a wing and fuselage, a straightforward application of the described algorithm can lead to a non-smooth or non-contiguous deformed wetted surface.

With configurations comprising more than one assembly, any projection between surface components and structural model parts not physically connected must be avoided. This is exemplified in Fig. 3 for a high-lift device. The structural elements closest to surface points along the trailing edge actually belong to the flap. Projections based solely on shortest distance lead to a physically impossible transfer of loads and deformations over the flap gap. This is prevented by explicitly assigning structural elements to surface segments of the individual assemblies. In a preparatory step all collinear beam elements of each assembly are combined in element groups. Each assembly's surface segment is given a unique identifier. In the ACM's input data set, the element groups are then either assigned to surface segments or excluded from the projection algorithm. In the current example, the flap track elements should be excluded because they have no wetted surface segments as counterparts for mapping.

However, the strict application of this explicit assigning can make the wetted surface come apart at intersections between assemblies: Due to their projection on

elements of different element groups, those neighbouring surface points which are part of different assemblies can experience incompatible deflections. The two surface segments necessarily contiguous in the undeformed configuration are no longer so after the deformation projection. The resulting defective mesh is not suitable any more for flow computations. This problem is resolved by means of an interpolation algorithm, which is exemplified by the wing-fuselage joint shown in the left image of Fig. 4. First, all seam curves between adjacent surface segments are detected. For a surface point belonging e.g. to the main wing, the projection is carried out onto the directly assigned element groups of the wing, giving a "direct" deflection $\mathbf{u}_{\mathrm{CFD}}^{\mathrm{dir}}$. Next, the projection is repeated for the element groups assigned to the neighbouring fuselage surface, which gives an "indirect" deflection $\mathbf{u}_{\mathrm{CFD}}^{\mathrm{indir}}$. The weighted average of the two contributions is taken:

$$\mathbf{u}^{\mathrm{CFD}} = \frac{1}{1+w_a}\,\mathbf{u}_{\mathrm{CFD}}^{\mathrm{dir}} + \frac{w_a}{1+w_a}\,\mathbf{u}_{\mathrm{CFD}}^{\mathrm{indir}} \qquad \text{with } w_a = w\left(\frac{a}{a_{\mathrm{limit}}}\right). \tag{3}$$

The distance a of the surface point from the seam curve normalised with the user-supplied width of the intersection region a_{limit} determines the interpolation weight. The weighting function w is a high-order polynomial. The interpolation assures a smooth deformed wetted surface where neighbouring points on opposite sides of a seam curve have compatible deflections. A comparable algorithm has been realised by Badcock et al. [2] inside the CVT method.

In the concave region enclosed by the beam kink valid projections on multiple beam elements are possible. If for each surface point projection on the closest element is applied exclusively, some adjacent surface points will be paired with projection points far apart from each other. Their differing deformation values will result in creases in the wetted surface, which are neither physically justified nor favourable for the flow solver. This problem has to be resolved with an additional interpolation algorithm, which is explained along the beam model with two kinks shown on the right of Fig. 4: For a given surface point, a projection is determined onto each element group. For each one, the surface point deflection $\mathbf{u}_{\mathrm{CFD},i}$ resulting from the structural deformation at the given projection point $\mathbf{P}_i$ is calculated and two interpolation weights are assigned. The first interpolation weight w_β is a function of the deviation β of the projection angles from a right angle. The second interpolation weight w_d is defined by the ratio of distances of the projection points to the surface point:

$$w_{\beta,i} = w\left(\frac{\beta_i}{\beta_{\mathrm{limit}}}\right), \qquad w_{d,i} = w\left(\frac{d_i/d_{\min}}{d_{\mathrm{limit}}}\right) \tag{4}$$

β_{limit} and d_{limit} are user-defined parameters which determine the extent of the interpolation region. The final surface point deflection is then interpolated from all considered projection results:

$$\mathbf{u}_{\mathrm{CFD}} = \sum_i w_{\mathrm{tot},i}\,\mathbf{u}_{\mathrm{CFD},i} \quad \text{with} \quad w_{\mathrm{tot},i} = \frac{w_{\beta,i}\,w_{d,i}}{\sum_j w_{\beta,j}\,w_{d,j}} \tag{5}$$

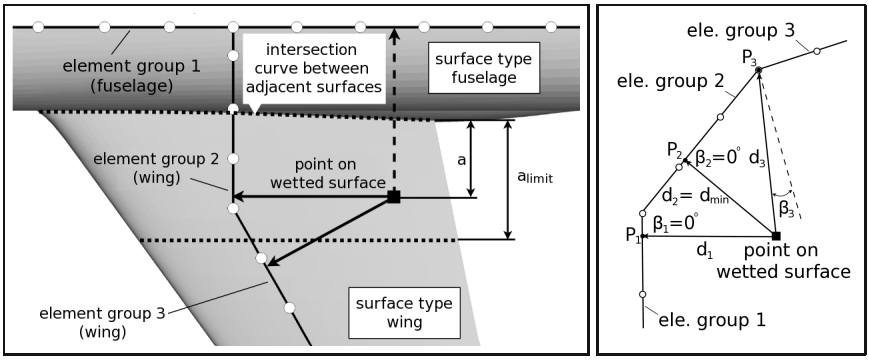

Fig. 4 *left:* Blending in the vicinity of intersections between surface segments of different assemblies, here at the wing-fuselage joint. *right:* Interpolation regions with non-unique mapping near kinks of the beam axis.

All interpolations have to be applied in the same manner also during the load projection as otherwise the conservativity would be violated (cf. Eq. (2)).

3.3 Global Spline-Based Interpolation (GSB)

As alternatives to the existing FIE scheme, in the project MUNA, the spatial coupling schemes GSB and MLS were implemented in the ACM. They are closely related, as both cast the problem of projecting loads or deformations as an interpolation problem: For a set of N points in space $\bar{\mathbf{x}}_n$ with dependent values $f(\bar{\mathbf{x}}_n)$ one seeks to find a functional approximation to f based on a suitable choice of interpolation functions. In this sense, the distribution of dependent values is the deformation $\mathbf{u}$ provided at the structural nodes. Its functional approximation is then evaluated at a second set of M points $\hat{\mathbf{x}}_m$, which are the points of the CFD surface mesh. The two projection methods differ in their choice of interpolation functions which dictates the solution process.

The GSB method was originally published by Beckert and Wendland [6]. The authors approximate the deformation on the whole domain with a global low-order polynomial with Q monomials. The monomial vectors are either

$$\mathbf{m} = (1,\, x,\, y,\, z)^T \quad \text{or} \quad \mathbf{m} = (1,\, x,\, y,\, z,\, x^2, y^2, z^2, xy,\, yz,\, zx)^T . \tag{6}$$

Superimposed are local contributions $\phi(\mathbf{x})$ that consist of radial basis functions (RBF). At a given coordinate, the interpolation function is

$$s(\mathbf{x}) = \mathbf{m}^T(\mathbf{x})\,\beta + \sum_{n=1}^{N_\delta} \alpha(\bar{\mathbf{x}}_n)\,\phi(\mathbf{x}, \bar{\mathbf{x}}_n) . \tag{7}$$

The coefficients $\alpha(\bar{\mathbf{x}}_n)$ of the local RBF contributions and the coefficient vectors $\boldsymbol{\beta}$ of the global polynomial are calculated simultaneously for all N_δ support points with a weighted least-squares algorithm. The dependent values at the interpolation support points are reproduced exactly. The RBFs with compact support constructed by Wendland [30] serve as weighting functions. The C^2-continuous Wendland-RBF with a support radius δ is provided here as an example:

$$\phi(\mathbf{x}, \bar{\mathbf{x}}_n) = (1-\tilde{x})_+^4 (4\tilde{x}+1) \quad \text{with} \quad \tilde{x} = \frac{1}{\delta} \|\mathbf{x} - \bar{\mathbf{x}}_n\|_2 . \tag{8}$$

The index $+$ marks that the factor $(1-\tilde{x})^4$ is set to zero for values of $\tilde{x} > 1$, whereby the compact support is realised. The functional approximation to the deformation distribution can be obtained from the linear system of equations

$$\underbrace{\begin{bmatrix} [\phi(\bar{\mathbf{x}}_i, \bar{\mathbf{x}}_j)] & [\mathbf{m}^T(\bar{\mathbf{x}}_i)] \\ [\mathbf{m}(\bar{\mathbf{x}}_j)] & 0 \end{bmatrix}}_{=\mathsf{C}} \begin{Bmatrix} \{\alpha_i\} \\ \boldsymbol{\beta} \end{Bmatrix} = \begin{Bmatrix} \{u_\lambda(\bar{\mathbf{x}}_j)\} \\ \mathbf{0} \end{Bmatrix}, \quad 1 \le i, j \le N_\delta , \tag{9}$$

which has to be solved for each Cartesian displacement component $\lambda = x, y, z$. (Here, scalar quantities that are combined to a vector are put in braces. Brackets denote that scalars or vectors that are assembled to form a matrix.) This process would have to be repeated in each coupling step; instead the inverse of the coefficients matrix C is determined. The functional approximation can now be evaluated at the surface points, which yields the final projection matrix P:

$$\begin{Bmatrix} \{u_\lambda(\hat{\mathbf{x}}_j)\} \\ \mathbf{0} \end{Bmatrix} = \underbrace{\left[[\phi(\hat{\mathbf{x}}_i, \bar{\mathbf{x}}_j)] \; [\mathbf{m}^T(\hat{\mathbf{x}}_i)] \right] \mathsf{C}^{-1}}_{\mathsf{P}} \begin{Bmatrix} \{u_\lambda(\bar{\mathbf{x}}_i)\} \\ \mathbf{0} \end{Bmatrix}, \tag{10}$$
$$1 \le i \le N_\delta \quad 1 \le j \le n_{\text{CFD}} .$$

In the GSB method the support radius δ has to be the same all over the computational domain, or else the interpolation scheme will not be consistent. In general, the number of support points N_δ will differ from one CFD surface node to the next. The user has to define a minimum required number of support points and the projection scheme searches the domain for the smallest radius δ that contains this number. Because of the global contribution to the interpolation function the resulting projection matrix is dense. Its definition here (and in the MLS method) differs from the definition in Eq. (2) in that here the deformations or forces are projected one spatial component λ at a time. The GSB method is largely identical to the volume mesh deformation method presented by Barnewitz in this volume. The main difference lies in the choice of weighting functions and the compact support of the local contributions to the interpolation function.

3.4 Moving-Least-Squares Interpolation (MLS)

The MLS interpolation method was first applied to spatial coupling in aeroelasticity by Quaranta et al. [23]. It exclusively uses low-order polynomials

$$s(\mathbf{x}) = \mathbf{m}^T(\mathbf{x})\,\boldsymbol{\alpha} \tag{11}$$

to approximate the spatial deformation distribution $\mathbf{u}(\bar{\mathbf{x}})$. At each CFD surface point $\hat{\mathbf{x}}$, a new set of Q polynomial coefficients $\boldsymbol{\alpha}(\hat{\mathbf{x}})$ is computed with a moving least-squares fit. The N_δ closest support points $\bar{\mathbf{x}}_n$ provide a compact support; their influence relative to the CFD surface point is weighted with Wendland RBF (8). For each surface point $\hat{\mathbf{x}}$ and its N_δ support points inside the support radius δ a functional

$$I(\hat{\mathbf{x}}, \bar{\mathbf{x}}_n) = \int_{\bar{\Omega}_\delta} \phi(\hat{\mathbf{x}}, \bar{\mathbf{x}}_n)\,\left(\mathbf{m}^T(\bar{\mathbf{x}}_n)\,\boldsymbol{\alpha}(\hat{\mathbf{x}}) - u_\lambda(\bar{\mathbf{x}}_n)\right)^2 d\Omega(\bar{\mathbf{x}}_n) \tag{12}$$

has to be minimised for the coefficients $\boldsymbol{\alpha}(\hat{\mathbf{x}})$. The discrete form of this functional is reduced to the normal equation through a variation of coefficients $\delta\boldsymbol{\alpha}$:

$$\underbrace{\left[\,[\mathbf{m}(\bar{\mathbf{x}}_n)]\,\Phi(\hat{\mathbf{x}}, \bar{\mathbf{x}}_n)\,[\mathbf{m}(\bar{\mathbf{x}}_n)]^T\,\right]}_{=\mathsf{A}}\,\boldsymbol{\alpha}(\hat{\mathbf{x}}) = \underbrace{\left[\,[\mathbf{m}(\bar{\mathbf{x}}_n)]\,\Phi(\hat{\mathbf{x}}, \bar{\mathbf{x}}_n)\right]}_{=\mathsf{B}}\,\{u_\lambda(\bar{\mathbf{x}}_n)\} \tag{13}$$

Herein, $\Phi(\hat{\mathbf{x}}, \bar{\mathbf{x}}_n) = \mathsf{E}\,\{\phi(\hat{\mathbf{x}}, \bar{\mathbf{x}}_n)\}$ is the diagonal matrix of RBF weighting factors. Inserting the interpolation function (11) yields

$$u_\lambda(\hat{\mathbf{x}}) = \underbrace{\mathbf{m}^T(\hat{\mathbf{x}})\,\mathsf{A}^{-1}\mathsf{B}}_{=\mathbf{P}(\hat{\mathbf{x}})}\,\{u_\lambda(\bar{\mathbf{x}}_n)\}\,. \tag{14}$$

The row matrix $\mathbf{P}(\hat{\mathbf{x}})$ describes the projection between a single surface point $\hat{\mathbf{x}}$ and the N_δ support points inside the support radius. Other than in the GSB method, in the MLS method the projection matrix is built row by row for each surface point separately. The final projection matrix P is assembled from the M row matrices of all surface points. For each surface point a $Q \times Q$-matrix A has to be set up and inverted. Its condition number and thus its invertability depends on the number of support points and their spatial arrangement. Practical experience has revealed that the regularisation of the linear systems of equations (13) by left multiplication of $[\mathbf{m}(\bar{\mathbf{x}}_n)]$ is highly detrimental to its condition number. A more accurate and robust numerical solution can be achieved if instead for each surface point the N_δ overdetermined systems of equations

$$\Phi(\hat{\mathbf{x}}, \bar{\mathbf{x}}_n)\,[\mathbf{m}(\bar{\mathbf{x}}_n)]^T\,[\boldsymbol{\alpha}^*(\bar{\mathbf{x}}_n)] = \Phi(\hat{\mathbf{x}}, \bar{\mathbf{x}}_n) \tag{15}$$

are solved with QR decomposition, yielding N_δ tuples of polynomial coefficients $\boldsymbol{\alpha}^*(\bar{\mathbf{x}}_n)$ for unit deflections $u^*_\lambda(\bar{\mathbf{x}}_n)$ at the individual support points. The final row entry to the projection matrix then is

$$\mathbf{P}(\hat{\mathbf{x}}) = \mathbf{m}^T(\hat{\mathbf{x}})\,[\boldsymbol{\alpha}^*(\bar{\mathbf{x}}_n)]\,. \tag{16}$$

Because the interpolation function (11) has only local support, the projection matrix is sparse, greatly reducing memory requirements in comparison with the GSB method.

Investigations using configurations with multiple components revealed that even with these new projection methods explicitly based on interpolation schemes additional interpolation in intersection regions between assemblies cannot be avoided. If the whole configuration is treated as a single assembly during the projection, the resulting deformed wetted surface is contiguous, but extremely distorted. (With the GSB method, its global polynomial term in the interpolation function can even result in an unfeasible propagation of deformations to assemblies not directly connected, e.g. from the main wing to the empennage.)

For the MLS scheme, an additional interpolation in intersection regions has been implemented that works in a similar fashion as the interpolation of the FIE method (3): For a surface point situated in an intersection region, as depicted on the left of Fig. 4, a row entry to the projection matrix $\mathbf{P}_k(\hat{\mathbf{x}})$ is built for the element groups directly assigned. Further entries are built with the structures of each adjacent surface segment. The resulting K row entries are assigned normalised weights w_k according to the surface point's distance a to the intersection curve. Weighted averaging yields the final entry to the projection matrix for the given surface point:

$$\mathbf{P}(\hat{\mathbf{x}}) = \sum_{k=1}^{K} w_k(\hat{\mathbf{x}}, a_{\text{limit}})\,\mathbf{P}_k(\hat{\mathbf{x}}) \quad \text{with} \quad \sum_{k=1}^{K} w_k(\hat{\mathbf{x}}, a_{\text{limit}}) = 1\,. \tag{17}$$

This interpolation algorithm exploits the fact that the MLS method builds the projection matrix one surface point at a time. In the GSB method, the projection matrix is created for all points simultaneously. To realise a comparable interpolation, for each assembly a projection matrix would have to be built which relates the points of its surface segment to all neighbouring structures. Only then the average can be taken with suitable weights assigned to the row entry of each surface point. Because of the high memory requirements of just a single projection matrix resulting from the GSB method, comparable interpolation has not been implemented in the ACM.

3.5 Insertion of Additional Support Points

The solution accuracy and the robustness of the MLS projection algorithm improves with increasing number of support points, but only if these offer sufficient information density in all spatial directions. Moreover, with higher number of support points necessarily also the support radius becomes larger; hence the desirable locality of the projection diminishes. These two problems can be alleviated by using an idea also put forward by Quaranta et al. [23]: It is not the actual nodes of the

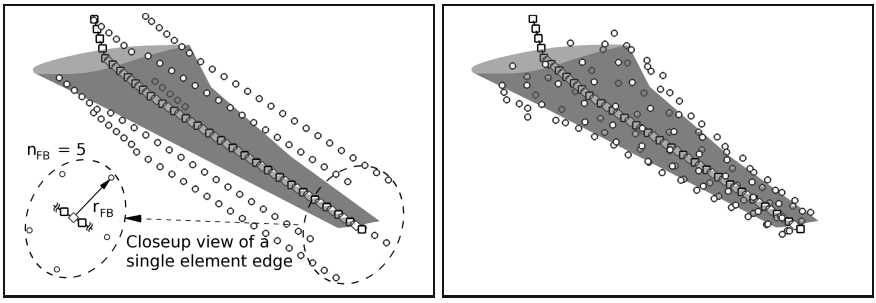

Fig. 5 *left:* Arrangement of the "fishbones" generated for a beam model. The structural nodes are represented by squares, the edge midpoints by diamonds and the additional support points by circles. Here the radius r_{FB} is fixed to a value approximately half the average chord length. The number of additional support points per edge midpoint n_{FB} is set to five, which is the recommended value for beam models. *right:* Arrangement of the additional support points after alignment with the wetted surface.

structural model that are taken as supports for the interpolation. Instead, the midpoints of the beam elements, or respectively the edge midpoints of higher-dimensional elements are used. Surrounding these points, additional supports are inserted circumferentially, as shown in the left image of Fig. 5. Quaranta et al. coined the term "fishbones" for this arrangement. The additional support points not only assure adequate information distribution in all spatial directions, but also allow for the simple projection of rotational deformational components at the structural nodes: The rotations are interpolated to the edge midpoints and result in a translation of the additional support points according to their radius r_{FB}. During the converse projection of loads from the wetted surface to the structure the forces projected to the additional support points are combined at the edge midpoints and corresponding offset moments are introduced. The loads at the edge midpoints are then split between the adjacent structural nodes.

The GSB and MLS projection methods were further enhanced by enabling an automatic alignment of the additional support points with the wetted surface, as shown on the right of Fig. 5. To this end, the information which surface points are in the vicinity of each edge midpoint is required. Therefore, in a preparatory step the mapping of supporting edge midpoints to surface points is inverted. The shape of the surface section normal to a given edge is approximated as an ellipse. The additional support points are then inserted along its circumference with equiangular spacing. Special attention is needed when the wetted surface does not cover the whole circumference, like along the fuselage of a half-model suspended in the symmetry plane.

4 Error Sources in Spatial Coupling

In this section, the investigation of error sources in the spatial coupling by means of model problems shall be detailed. Tracing the steps outlined in Section 2, several potential sources of error were identified and looked into during the project MUNA. Three of these investigations are presented here: The influence of the mesh spacing of the structural and surface mesh is determined as well as the effect of the deformation mapping on the shape of the deformed wetted surface. For all three available spatial coupling methods, parameter studies were carried out to ascertain the importance of the user-defined projection parameters.

4.1 CFD Mesh Spacing and Load Distribution

When discretising the solution domains of the flow problem and of the structural problem before a coupled aeroelastic simulation, one would prefer to choose the grid spacings only considering the requirements of the single-field solvers and the desired solution accuracy. Especially one would like to avoid having to match up the discretisations at the coupling surface, which might not be possible at all when reduced structural models are used. Therefore the question arises as to how the choice of mesh spacings of the structural model and of the subsets of the CFD volume mesh representing the wetted surface influence the projection results. The influence on the load projection is most conveniently analysed by regarding the calculation of the consistent nodal loads on the wetted surface together with their projection on the structure.

4.1.1 One-Dimensional Test Setup

First investigations were carried out with one-dimensional test configurations loosely following an approach laid out by Jaiman et al. [17]: The one-dimensional fluid mesh and the structural mesh are colinear, but feature non-matching discretisations. An analytical pressure distribution is applied to the fluid mesh. The equivalent consistent nodal loads are then projected on the structural nodes. Furthermore, a reference load distribution can be obtained by calculating the nodal loads consistent with the pressure distribution directly at the structural nodes. The reference loads can then be used to calculate a relative error ε_F of the projected loads. In the first three diagrams of Fig. 6, the analytical pressure distribution is plotted over the length of the one-dimensional domain together with the forces acting on the fluid nodes and on the structural nodes. The fluid mesh is discretised with an increasing number of elements n_{CFD}, whereas the number of elements on the structural side is kept constant at $n_{CSD} = 20$. In this example, linear shape functions are used for both the calculation of the consistent nodal forces and for their projection with the FIE method. With the coarser CFD meshes the distribution of the projected forces on the structural nodes is highly irregular. Parameter studies indicate that the mesh spacings on

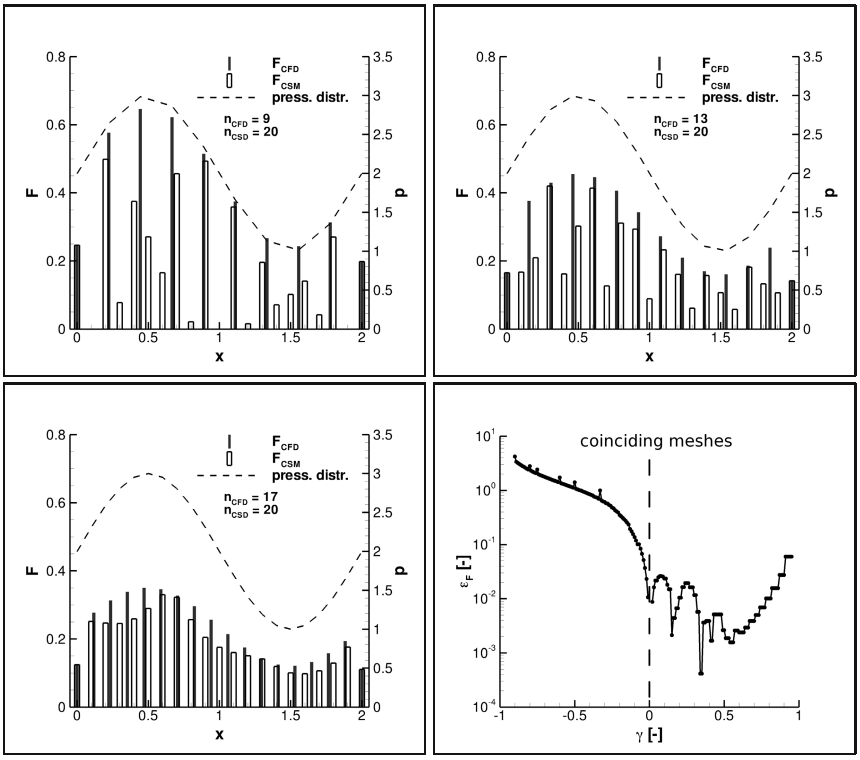

Fig. 6 Influence of the mesh ratio on the load distribution on a one-dimensional test configuration. *top left, top right and bottom left:* Consistent nodal forces on the fluid nodes and projected forces on the structural nodes for fluid meshes with 9, 13 and 17 elements. The number of structural elements is kept at $n_{\mathrm{CSD}} = 20$. *bottom right:* Relative error ε_{F} plotted over the mesh ratio γ.

both sides have to be fairly similar in order to achieve a sufficiently regular load distribution. The graph on the bottom right of Fig. 6 underscores this result. It shows the relative error plotted over the mesh ratio $\gamma = \frac{1-n_{\mathrm{CSD}}/n_{\mathrm{CFD}}}{1+n_{\mathrm{CSD}}/n_{\mathrm{CFD}}}$. Values from -1 to 0 imply a fluid mesh coarser than the structural mesh, and values between 0 and 1 a finer one. For negative values of γ the error is high, and only approaching $\gamma = 0$ it decreases to an acceptable level. In this example, for $\gamma = 0$ the structural nodes and the fluid nodes are placed at the same coordinates and the relative error becomes zero (not shown in the logarithmic diagram).

4.1.2 Beam Model Test Setup

While these studies revealed first clues of the influence of the structural and CFD surface mesh spacings, the test configuration is very abstract and the conclusions

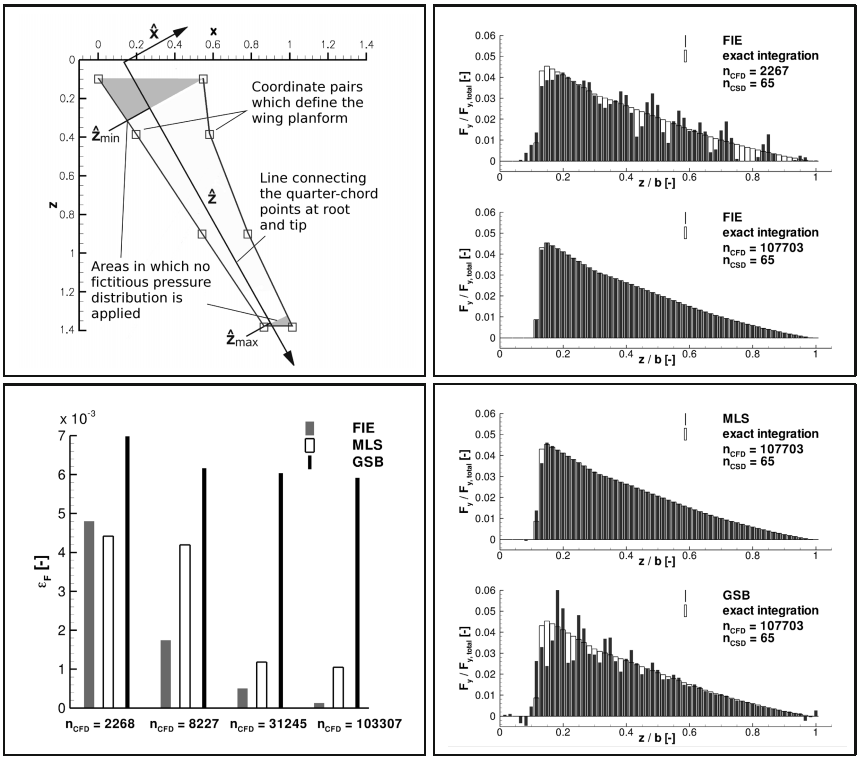

Fig. 7 Influence of the CFD mesh resolution on the structural load distribution. *top left:* Definition of the fictitious pressure field imposed on the wing. *top right:* Nodal forces in flap-wise direction resulting from the pressure distributions on the coarsest and the finest surface mesh and the projection with FIE. These loads are juxtaposed with those obtained by exact integration of the pressure distribution. *bottom left:* RMS error of the nodal forces in flap-wise direction for the three projection methods. *bottom right:* Nodal forces in flap-wise direction resulting from the pressure distributions on the finest surface mesh and projection with MLS and with GSB.

may not be transferable to real-world problems. Further test configurations were created for use together with the stand-alone version of the ACM which are based on the wetted surface of the HIRENASD wing [4]. The resolution of the wetted surface was varied again to quantify its effect on the structural load distribution. Four refinement levels with 2268, 8227, 31245 and 107703 nodes were realised by extracting different multigrid levels from a structured FLOWer mesh. Certainly, with an actual flow solver any change of the mesh alters the flow solution. Because this problem is specific to the single-field solver and not to the spatial coupling method, a fictitious pressure distribution was again employed here. It is defined in terms of the rotated planform coordinates $(\hat{x}, \hat{z})$ shown on the top left of Fig. 7. The $\hat{z}$-axis is chosen to connect the quarter-chord points at root and tip. The pressure distribution describes a quarter cosine wave along the $\hat{z}$-axis and half a sine wave along

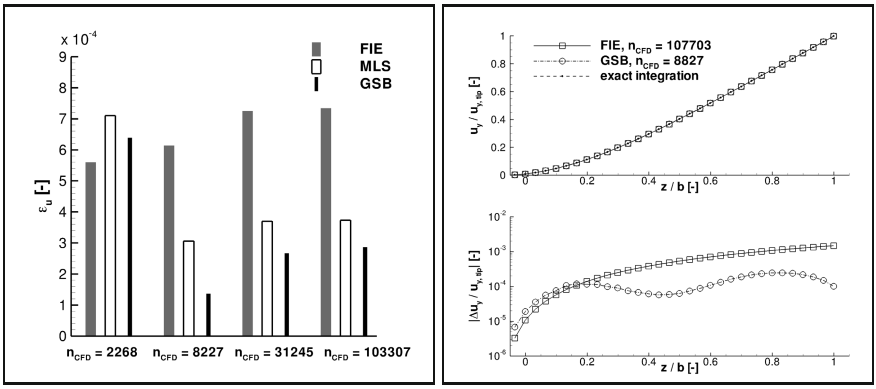

Fig. 8 Influence of the CFD mesh resolution on the structural deformation. *left:* RMS error of the flapwise bending deflections resulting from the different load distributions. *right:* Comparison of the actual bending deflections and the distributed error for the case with the highest deflection error (FIE, $n_{\mathrm{CFD}} = 103307$) and the lowest (GSB, $n_{\mathrm{CFD}} = 8227$).

the perpendicular coordinate direction $\hat{x}$. In the shaded areas the fictitious pressure distribution is zero. It is applied with opposite signs to both surfaces of the wing to produce a net positive bending moment in flap-wise direction. From the exact integration of the pressure distribution a line load along the $\hat{z}$-axis is obtained. If a beam stick model has parallel orientation, the line load can be divided consistently among the structural nodes to obtain a reference load distribution. This serves to define an error incurred by each projection scheme in dependence of the surface mesh resolution. Moreover, with the reference load distribution the structural deformation is computed and compared to those of the projected loads. As a measure for the error the root mean square (RMS) of the nodal forces in flap-wise direction, normalised by the total force in flap-wise direction, is used:

$$\varepsilon_{\mathrm{F}} = \sqrt{\frac{1}{n_{\mathrm{CSD}}} \sum_{i=1}^{n_{\mathrm{CSD}}} \left(\frac{F_{y,i} - F_{y,i,\mathrm{exact}}}{F_{y,\mathrm{tot}}} \right)^2} \quad \text{with} \quad F_{y,\mathrm{tot}} = \sum_{i=1}^{n_{\mathrm{CSD}}} F_{y,i,\mathrm{exact}} \,. \tag{18}$$

This is plotted in the bottom left image of Fig. 7 and different trends are apparent for the projection schemes. FIE exhibits a strong reduction in the error when the surface mesh resolution is increased, whereas the error with GSB remains almost constant. MLS ranges in between. In contrast to the FIE method the MLS and GSB methods are not able to capture the discontinuous onset of the pressure distribution near the root because they rely on finite support radii. Even with the finest surface mesh the load distribution at the root remains smeared out. Over the remaining span the MLS method approximates the exact loads well, whereas with the GSB method there are still large discrepancies, as can be seen from the bottom right diagrams of Fig. 7. In the left image of Fig. 8 the resulting bending deflections in flap-wise directions are compared by means of the RMS differences of the nodal deflections normalised by the tip deflection

$$\varepsilon_{\mathrm{u}} = \sqrt{\frac{1}{n_{\mathrm{CSD}}} \sum_{i=1}^{n_{\mathrm{CSD}}} \left(\frac{u_{y,i} - u_{y,i,\mathrm{exact}}}{u_{y,\mathrm{tip}}} \right)^2}. \tag{19}$$

It should be noted that because of their different normalisation the error values ε_{u} and ε_{F} cannot be directly compared.

For the investigated straight beam model, the differences in the load distribution do not translate in large differences in deformations. This is documented in the right diagram by a comparison of the bending deflections and their deviations from the reference distribution for the cases with the highest and the lowest total deflection error. The deformed structural models are almost identical because in all projection methods the redistribution of the bending forces along the beam axis is compensated by offset moments.

As the structural model is straight and the configuration comprises only a single assembly, no interpolation parameters come into play with the FIE method (cf. Chap. 3.2). For both the MLS and the GSB method, eight edge midpoints were set as supports, with $n_{\mathrm{FB}} = 5$ additional support points each. The radius of the support points was chosen as $r_{\mathrm{FB}} = 0.15$ m, which is approximately half the mean chord length. Quadratic polynomials were used for the global contribution to the interpolation function of the GSB method and for the local interpolation functions of the MLS method.

4.1.3 Shell Model Test Setup

With the beam model test configuration, the different interpolation schemes and surface mesh resolutions do not produce profound local load incidence effects or major differences in the global deformation. A third test setup was investigated which bears more resemblance to a real-world configuration. The wetted surface is the HIRENASD wing scaled to a half-span of 29 m. The structural model is a shell model kindly supplied by the Institute of Aircraft Design and Lightweight Structures (IFL) of the Technical University of Braunschweig. It is akin to a modern transport aircraft wing box and has been dimensioned to real-world design loads. As such it has a realistic ratio of local sheet flexibility to total cantilever flexibility. The model is depicted in the left image of Fig. 9; a detailed description can be found in the contribution of Reich et al. in this volume. Also in this test case on wetted surfaces with varying resolutions a fictitious pressure distribution was applied. However, it cannot be exactly integrated here and thus no reference load or deformation distribution is available. In the right image of Fig. 9, the loads projected on the structure with the MLS method are depicted for the coarsest and the finest surface mesh. With decreasing number of points on the wetted surface, the absolute values of the aerodynamic surface loads increase due to the larger area of each individual surface cell. At least for the structured CFD meshes used here, simultaneously a concentration of the surface loads occurs. Potentially both can cause local load incidence effects, i.e. local “bumps” on the shell model which are then projected back to the wetted surface and might locally alter the flow field. The bumps are a

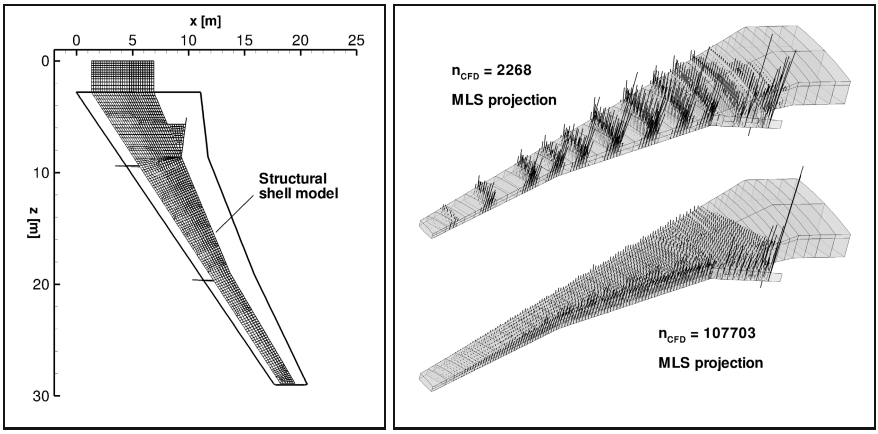

Fig. 9 *left:* Planform of the scaled HIRENASD wing and structural shell model created at the Technical University of Braunschweig. *right:* Comparison of the force vectors resulting from the fictitious pressure distribution on the coarsest and on the finest wetted surface and projection with MLS.

result of the mismatch between the structural and fluid meshes; if forces rather than surface strains are projected, any such appearance must be examined: does it represent a valid structural deformation or is it merely an artifact of the spatial coupling method.

In Fig. 10 the deviations in load and deformation distributions are compared for the FIE and MLS projection and the four investigated surface meshes. No results were obtained with the GSB method owing to the high numerical effort brought about by the inversion of the RBF weights matrix C in Eq. (10). The data plotted in Fig. 10 are not be understood as absolute projection errors. The reference values do not result from exact solution, which is not available. Here, the results obtained for the surface mesh with 107703 points and the FIE method were chosen, this however does not implicitly make them the "correct" values.

In the top left diagram there is an inherent deviation visible between the load distributions obtained with the projection methods which does not decrease significantly with increasing mesh resolution. The deviations in the deformation distribution, though, are strongly dependant on the mesh resolution rather than on the projection method, as can be seen from the top right diagram. This effect can once again be attributed to the offset moments which partially compensate the differences between the load distributions. A distributed deformational deviation was extracted along a line in span-wise direction and is shown in the bottom left image of Fig. 10. The graphs for the coarsest surface mesh and projection with FIE and MLS are virtually identical. They exhibit the mentioned bumps, but also a global bending deflection higher than in the reference case. The bumps are in the order of tenths of a per cent of the total bending deflection, which for this model equates to local

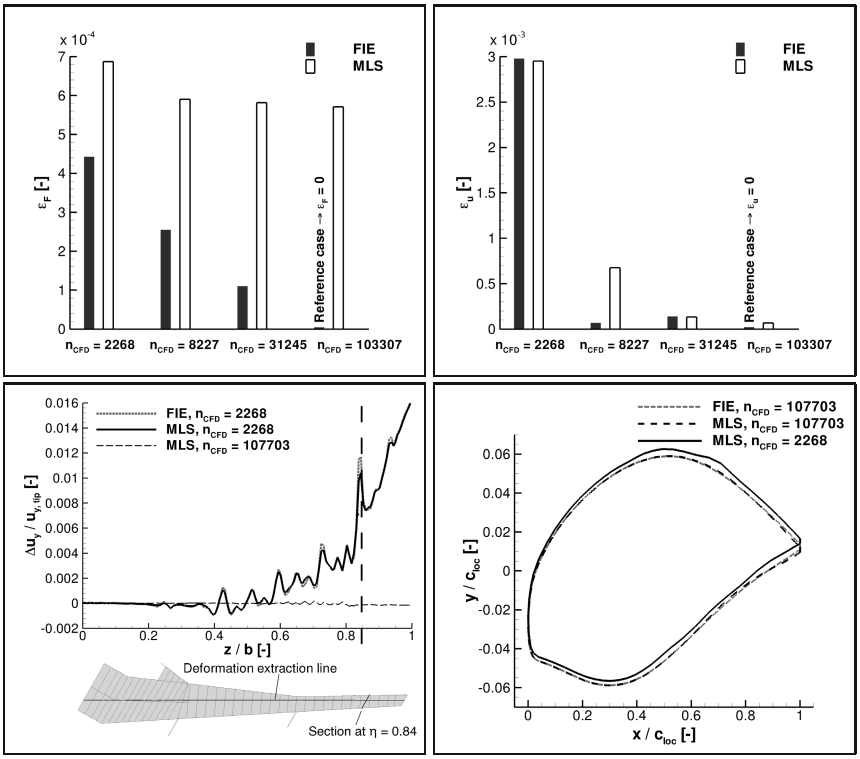

Fig. 10 *top left:* RMS deviations of the forces in flap-wise bending direction according to Eq. (18). In all plots shown in this panel the finest wetted surface with 107703 nodes and FIE projection provides the reference values. *top right:* RMS deviations of the flap-wise bending deflections according to Eq. (19). *bottom left:* Local deviations of the bending deflection in flap-wise direction for the coarsest surface mesh and projection with MLS and FIE. The deflections are extracted along the length of the suction side of the wing box. Additionally the deviations with the finest surface mesh and MLS projection are shown. *bottom right:* Comparison of sections through the wetted surface at the spanwise position $\eta = 0.84$.

differences in the contour of several millimetres. The difference in global deflection is in the order of one per cent. The deviations between the projection methods for the finest mesh level are also plotted. They are close to zero all along the span. For a rough assessment of the influence of the differing structural deformations on the shape of the wetted surface, in the bottom right image two sections through the wetted surface at the spanwise position $\eta = 0.84$ are superimposed, which is where the distinct peak in the deviations is visible in the bottom left image. This comparison is slightly marred by the fact that the respective projection methods are applied twice, first for the loads and again for the deflections. Nonetheless, both the difference in global deflection and a bump on the suction side are apparent for the coarsest wetted surface. It can be concluded that with thin-walled structural shell models and coarse

CFD meshes load incidence effects can indeed have an influence on results, but it is seen to diminish rapidly with the finer CFD meshes. Even though such coarse meshes are not regularly used for standard steady simulations, they still play a role in unsteady simulations and in design, where accuracy is sacrificed for the sake of solution speed. For instance during the preceding project MEGADESIGN [20], a design case was investigated using a volume CFD mesh with approximately 170000 points; 4425 points thereof made up the surface mesh.

4.2 Influence of Projection Parameters

The spatial coupling methods available in the ACM all base the transfer of loads and deformations on geometric neighbourhood relations between the wetted surface and the structure. For this, the methods require different additional interpolation parameters. As explained in Chap. 3.2, the FIE method for beam elements has three additional interpolation parameters: The weighting parameters β_{limit} and d_{limit} apply for projections of surface points in the vicinity of kinks of the beam model. The width of the intersection region a_{limit} has to be defined if assemblies border on each other. For shell and volume models, the FIE method currently does not call on interpolation parameters. Once it has been extended to configurations with multiple assemblies, a_{limit} also will come into play. The GSB and the MLS methods are derived from general interpolation algorithms. They require the definition of the (minimum) number of supports N_δ or N_M, the number of additional support points per edge midpoint n_{FB}, their radius r_{FB}, the polynomial degree of the interpolation functions (7) or (11) and the type of RBF function ϕ. The MLS method is also suitable for configurations with multiple assemblies and thus again a_{limit} has to be provided. None of these parameters is directly based on physical considerations, so the optimal values are not obvious.

All interpolation parameters of the FIE method required for beam models shall be examined here, whereas for the MLS and GSB methods only a selection is presented in detail. As became clear from the results presented in Chap. 4.1.2, distinct load distributions can result in identical deformation distributions. Therefore, the influence of the projection parameters is evaluated via the deformation projection. In order to have identical input data for all cases, no aerodynamic loads are imposed on the wetted surface. Instead, a force distribution is applied directly to the structural nodes. The structural deformations then become independent of the projection method. The differences in the shape of the wetted surface can consequently be attributed solely to the deformation projection. Also in this investigation exact reference solution is not available, and as in the previous chapter the deviations should not be interpreted as absolute errors.

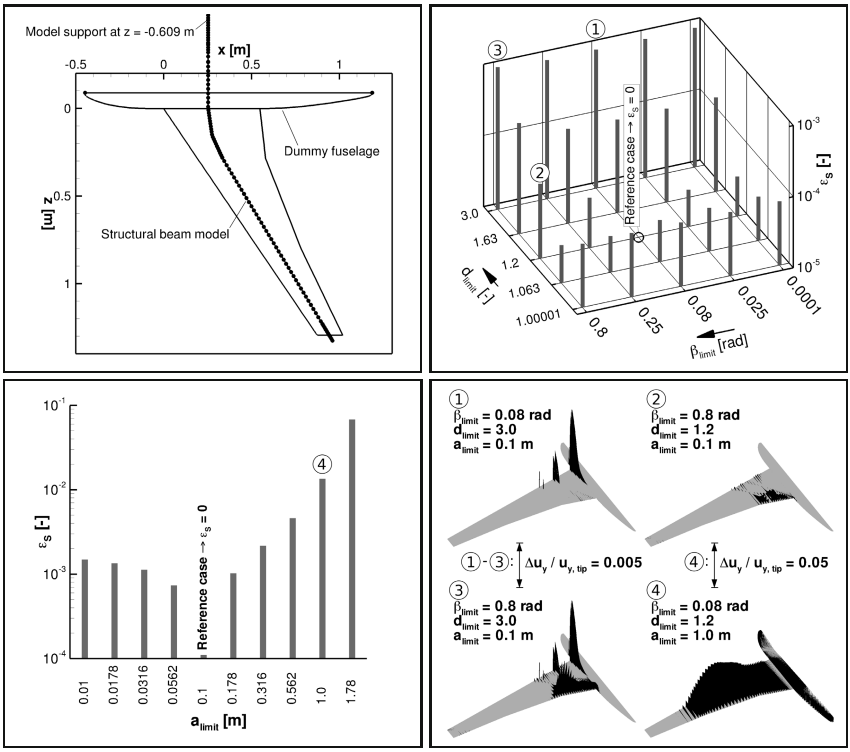

Fig. 11 *top left:* Planform of the HIRENASD wing and its structural beam model. The model support is outside the pane at $z = -0.609$ m. The dummy fuselage is not physically connected to the wing. It is also represented as a component in the beam model, but its nodes are all clamped. *top right:* RMS deviations of the wetted surface deflections relative to those obtained with the default settings. The parameters β_{limit} and d_{limit} are varied and a_{limit} is kept constant at 0.1 m. *bottom left:* RMS deviations of the wetted surface deflections relative to those obtained with the default settings. a_{limit} is varied, while the remaining parameters are kept constant at $\beta_{\text{limit}} = 0.08$rad and $d_{\text{limit}} = 1.2$. *bottom right:* Distributed values of the normalised deflection difference $|\Delta u_y / u_{y,\text{tip}}|$ for the four parameter combinations marked in the top right and bottom left diagrams.

4.2.1 Interpolation Parameters of the FIE Method for Beam Models

The interpolation parameters of the FIE method are the angular limit of the interpolation area in the vicinity of beam kinks β_{limit}, the limit ratio of projection distances in the vicinity of beam kinks d_{limit}, and the width of the intersection region between assemblies a_{limit}. They are varied and their respective influence on the shape of the deformed wetted surface is assessed. The test case is the HIRENASD configuration with a dummy fuselage, which constitutes a second assembly next to the wing. The CFD surface mesh sketched in the top left of Fig. 11 has 46919 points and the structural beam model has 654 nodes. These components are subjected to forces and moments which resulted from a previous aeroelastic simulation. These are kept

constant during the parameter study. The deformed wetted surface acting as a reference for the deviations was obtained with the default settings of the ACM, which are $\beta_{\text{limit}} = 0.08\,\text{rad}$, $d_{\text{limit}} = 1.2$ and $a_{\text{limit}} = 0.1$ m. This last value amounts to approximately 8% of the model half-span of 1.29 m. As the parameters d_{limit} and β_{limit} both relate to the interpolation in the vicinity of kinks, these parameters are studied together. The RMS deviation of the surface point coordinates ε_{S} is determined by analogy to ε_{u} as defined in Eq. (19). Also in this case only the differences in the flap-wise deflection are considered.

In the top right diagram of Fig. 11 the RMS deviations of the normalised deflection are plotted over the investigated parameter combinations. Whereas the minimum valid values of β_{limit} and d_{limit} are defined inside the ACM, the upper values were chosen arbitrarily. The choice of d_{limit} has a more profound effect on the shape of the wetted surface than β_{limit}. There is a weak interdependence visible between the two parameters. The indication of a global RMS value is somewhat misleading here, as both parameters lead to highly localised deviations. This can be seen in the bottom right image. The distributed values are displayed as bars over the configuration's planform for combinations of the maximum and the default settings of β_{limit} and d_{limit}. Distinct peaks close to the leading edge are apparent for the maximum value of d_{limit}, whereas for the maximum value of β_{limit} there are differences visible in the wedge-shaped areas of non-unique projection mentioned in Chap. 3.2. The choice of the width of the intersection region between fuselage and wing not only has a more widespread influence. It also produces deviations an order of magnitude higher and it thus gives far higher RMS errors. To put the given normalised distributed values into perspective: Assuming a bending deflection of 5% of the model half-span of 1.29 m, the peak deviation for parameter combination ③ is less than 0.5 mm, but for setting ④ with $a_{\text{limit}} = 1.0$ m it exceeds 3 mm.

4.2.2 Interpolation Parameters of the MLS and GSB Methods

The newly-implemented projection methods MLS and GSB have more control parameters than the FIE method. Only the (minimum) number of supporting edge midpoints N_M, the polynomial order of the interpolation functions and the radius of the additional support points r_{FB} are examined here. The results for the remaining parameters are briefly summarised beforehand. As reference for the deviations the deformed wetted surface obtained by application of the FIE projection with default parameter settings is used.

The number of additional support points to be generated around each edge midpoint n_{FB} depends on the type of structural model. In previous extensive tests, $n_{\text{FB}} = 5$ was determined as the recommended number for beam models. With lower numbers reliable solutions could neither be obtained with the MLS method nor with the GSB method. Then again, greater numbers do not yield noticeable improvements in robustness or accuracy. With structural models consisting of higher-dimensional elements, the number of additional support points generally can be reduced. For shell models $n_{\text{FB}} = 2$ is often sufficient. For volume models, additional support

points are likely to be omitted. The choice of the RBF has only very small influence on the solution both in the MLS and the GSB method. Wendland RBFs with different orders of smoothness have been tried out as well as other RBF with compact support, like Euclid's hat functions or the Thin Plate Spline, with hardly any effect on the wetted surface. Because the mechanism to perform the interpolation in intersection regions between assemblies in the MLS method is very similar to the mechanism in the FIE method, the same effects on the wetted surface can be expected from variations of a_{limit}.

The configuration used here is similar to the one presented in the previous section in Fig. 11, but without the dummy fuselage. It comprises only one component and thus allows direct comparison between GSB and MLS. The surface mesh has 31245 points. The structural model with 654 nodes and the applied load distribution are the same as before.

4.2.3 Interpolation Parameters of the GSB Method

In the top left image of Fig. 12, the RMS deviations in the flap-wise bending deflection are plotted over the minimum number of supporting edge midpoints $N_{M,\min}$. The radius of the additional support points was fixed at $r_{\text{FB}} = 0.15$ m. In the GSB method the actual number of support points differs all over the wetted surface, as was explained on page 193. The support points of a given surface point are all the edge midpoints and additional support points within the support radius δ. The deformed wetted surface used here as a reference was obtained with the FIE method and its default parameter settings. The deviations do not seem to be influenced by the number of support points. The RMS values hover at 1.7% for linear global interpolation functions and at 0.12% for quadratic ones. Yet the wetted surfaces obtained with MLS are not completely identical, as is documented in the bottom left diagram. It shows the RMS deviation relative to the deformed surface resulting from the GSB method with $N_{M,\min} = 8$. These deviations, however, are at least one order of magnitude smaller than those relative to the FIE reference case.

The top right image of Fig. 12 shows the influence of the radius of the additional support points. Eight fixed radii are investigated as well as the alignment of the additional support points with the wetted surface. The number of supporting edge midpoints is $N_{M,\min} = 8$; the reference wetted surface as before resulted from the FIE method. The better the spatial arrangement of the additional support points approximates the wetted surface, the lower the average deviations come to be. For both linear and quadratic global contributions to the interpolation function the smallest RMS values are achieved with an alignment of the additional support points. Next best is $r_{\text{FB}} = 0.15$ m, which is approximately half the mean chord length. Between $r_{\text{FB}} = 0.276$ m and $r_{\text{FB}} = 0.474$ m a marked increase in deviations occurs. This is because r_{FB} becomes larger than the fixed support radius δ, and the additional support points cease to come into play. Case ④ in the bottom right image shows the distribution of the normalised deviations. These increase over the length of the span and values of $|\Delta u_y / u_{y,\text{tip}}| > 2$ are reached at the tip. Cases ① and ② highlight a general

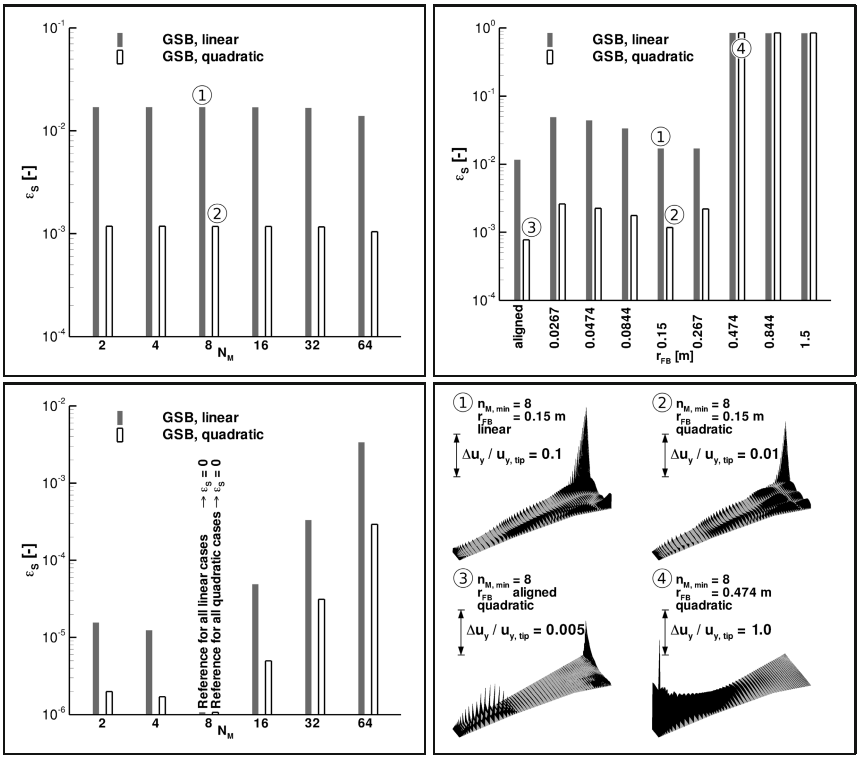

Fig. 12 RMS deviations of the wetted surface deflections of the GSB method relative to those obtained with the FIE method and its default parameter settings for the projection parameters. *top left:* Variation of the minimum number of supporting edge midpoints between $N_M = 2$ and $N_M = 64$ with $r_{\mathrm{FB}} = 0.15$ m. *top right:* Variation of the radius of the additional support points between $r_{\mathrm{FB}} = 0.0267$ m and $r_{\mathrm{FB}} = 1.5$ m with $N_M = 8$. *bottom left:* Variation of the minimum number of supporting edge midpoints between $N_M = 2$ and $N_M = 64$. In this diagram the deflected surface obtained with GSB and $N_M = 8$ is the reference for the deviations. These are determined separately for linear and quadratic global contributions to the interpolation function. *bottom right:* Distributed values of the normalised deflection difference $|\Delta u_y / u_{y,\mathrm{tip}}|$ for the four parameter combinations marked in the top diagrams. Note the different scales for each case.

problem of the GSB method: The deformation distribution is generally not approximated well by the global polynomial contribution to the interpolation function, not even by a quadratic one. This is to be compensated by the local RBF contributions of the edge midpoints and of the additional support points. The deviations become large in regions of the wetted surface far-off the support points, for instance at the leading and trailing edges. Consequently, case ③ with alignment of the additional support points with the wetted surface reveals significant improvement over cases with fixed values of r_{FB}.

Ahrem et al. [1] propose breaking down the configuration into sections and applying the GSB method on each one by itself. The projection results are smoothly interpolated by a partition of unity algorithm. In each section a different fit for the global polynomial contribution is obtained which results in a better approximation of the wetted surface. Simultaneously the memory requirements and the numerical effort are reduced. The downside is the introduction of yet another interpolation scheme, and this approach has not been included in the ACM.

4.2.4 Interpolation Parameters of the MLS Method

The parameter variations presented for the GSB method were repeated with the MLS method. In the top left image of Fig. 13 the RMS deviations are shown in dependence of the number of support midpoints N_M. As before the reference deformed wetted surface is provided by the FIE method with default parameter settings. In the MLS method, during selection of support points an edge midpoint is always considered jointly with its surrounding additional support points. Hence the total number of support points of a given surface point is always a fixed multiple of the supporting edge midpoints $N_\delta = (n_{\mathrm{FB}} + 1) \times N_M$, at least outside of intersection regions. For two edge midpoints the MLS projection with quadratic interpolation functions fails; the resulting deformed wetted surface is completely distorted. Even with the numerically more robust formulation (15) the MLS method requires a minimum number of support points which should be at least twice the number of monomials Q. With four or more supporting edge midpoints the MLS method results in only small deviations relative to the FIE method. Neither with linear nor with quadratic interpolation functions does the deviation exceed 10^{-4}. In the inset of the top left diagram, a typical distribution of the normalised deflection differences $|\Delta u_y / u_{y,\mathrm{tip}}|$ is given. These are present all over the wing. The finite support radius of the MLS method slightly smears the deformation during projection as compared to the FIE method's. This represents a systematic discrepancy largely independent of the choice of MLS parameters. There are minor differences between the resulting wetted surface, though, as can be seen from the top right diagram. Here, the deformed wetted surface obtained with MLS for $N_M = 8$ and $r_{\mathrm{FB}} = 0.15$ m is the reference. The different approximation orders of the interpolation functions are weakly reflected in the RMS values, as is the number of support points.

In the bottom images of Fig. 13 the influence of the radii of the additional support points is examined. The bottom left diagram underscores the systematic discrepancy between FIE and MLS which goes completely unaffected by the choice of r_{FB}. Again the smeared projection of deformations with MLS is apparent in the inset. The largest deviations occur in the region of the beam kink, where the shape of the surface deformed with FIE also depends on the choice of projection parameters (see cases ① to ③ in Fig. 11). In the bottom right diagram of Fig. 13, the deformed wetted surface obtained with MLS and $N_M = 8$ and $r_{\mathrm{FB}} = 0.15$ m is again the reference. For all contemplated parameter settings the deviations are very small. The systematic discrepancy between the results for linear and quadratic interpolation functions is due to the single peak at the leading edge wing root visible in the

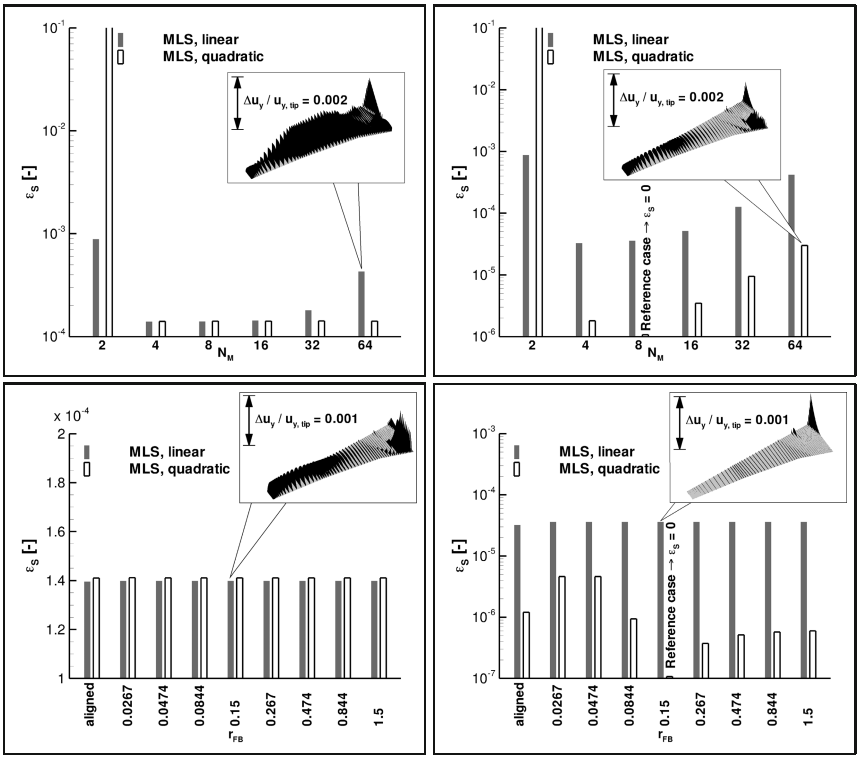

Fig. 13 RMS deviations of the wetted surface deflections of the MLS method. *top left:* Variation of the minimum number of supporting edge midpoints between $N_M = 2$ and $N_M = 64$ with $r_{\mathrm{FB}} = 0.15$ m. The deflected surface obtained with FIE and default parameter settings is the reference for the deviations. *top right:* Variation of the minimum number of supporting edge midpoints between $N_M = 2$ and $N_M = 64$. The deflected surface obtained with MLS and $N_M = 8$ and $r_{\mathrm{FB}} = 0.15$ m is the reference for the deviations. *bottom left:* Variation of the radius of the additional support points between $r_{\mathrm{FB}} = 0.0267$ m and $r_{\mathrm{FB}} = 1.5$ m with $N_M = 8$. The deflected surface obtained with FIE and default parameter settings is the reference for the deviations. *bottom right:* Variation of the radius of the additional support points between $r_{\mathrm{FB}} = 0.0267$ m and $r_{\mathrm{FB}} = 1.5$ m with $N_M = 8$. The deflected surface obtained with MLS and $N_M = 8$ and $r_{\mathrm{FB}} = 0.15$ m is the reference for the deviations.

inset of the bottom right image. This peak can be traced to the lack of additional support points in its vicinity, as can be identified in Fig. 5.

4.2.5 Comparison of the Projection Methods

The projection methods FIE, GSB and MLS were applied to similar configurations and at least a tentative comparison of their relative merits is possible. The projection mechanism of the FIE method is completely in line with beam theory in regions

Table 1 Memory consumption and execution time of the ACM with the available projection methods. Runs were carried out on a single 3.0 GHz Intel Xeon processor. The memory requirements include the storage of the system matrices and the solver workspace.

Configuration	HIRENASD wing with 31245 surface points, beam model with 653 structural elements			Scaled HIRENASD wing with 31245 surface points, shell model with 9352 structural elements	
Projection method	FIE	MLS	GSB	FIE	MLS
Duration of first coupling iteration [s]	3.40	3.47	258.84	204.88	86.29
Duration of subsequent coupling iterations [s]	0.06	0.05	1.45	0.86	0.80
Peak total memory requirement [MByte]	38.8	135.0	1617.6	1727.1	1740.3

where the beam axis is straight and does not have intersections. For the investigated test configuration, this region is the outboard part of the wing. In the vicinity of the beam kink the choice of the projection parameters β_{limit} and d_{limit} has a moderate influence on the local shape of the deformed wetted surface. Correct or optimal values for either are hard to ascertain, and the default values are the results of experience. Approximate values for the width of the intersection region a_{limit} can be determined by common sense, but the choice has a more profound effect on the shape of the wetted surface. While not shown here, fundamentally the same behaviour regarding a_{limit} can be expected for the MLS method. This method has the advantage that the number of support points n_δ and the radius of the additional support points r_{FB} can be varied over a large range with only marginal effects on the shape of the deformed wetted surface, independently of the polynomial order of the interpolation function. Compared to the FIE results the deformation distributions are slightly smeared during projection. Further differences to the FIE results are visible in the vicinity of kinks where the FIE method does not present a valid absolute reference either. Finally, the GSB method exhibits the strongest dependency on the choice of projection parameters. A high polynomial order of the global contribution to the interpolation function is beneficial, as it should already represent the deformation field as well as possible. The local RBF contributions have to make up for the difference between the supplied deformation distribution and its global approximation, so that the placement and number of supports bear a special importance.

From the user perspective, any projection method should not only be robust and deliver accurate results, but also have low computational resource requirements. The FIE method needs the least memory because in the implementation used in the ACM it does not store the projection matrix explicitly. The MLS method does so, but the resulting matrix is sparse. Discounting additional entries due to interpolation in intersection regions, the number of non-zero entries is $n_{\text{CFD}} \times N_\delta = n_{\text{CFD}} \times N_M \times (n_{\text{FB}} + 1)$. With the GSB method though, the projection matrix is dense

and the number of non-zero entries is the product of n_{CFD} and the total number of support points. It is also the method associated with the greatest numerical effort. In Table 1, typical run-times and peak total memory requirements are summarised for the test cases treated in Chapters 4.1.3 and 4.2. With the shell model, the memory requirements are dominated by the structural system and preconditioning matrices. The overhead for the explicit storage of the projection matrix of the MLS method is not significant, as opposed to the beam model test case.

5 Coupled Simulations

In order to assess the influence of the projection method on the actual coupled solution, steady aeroelastic simulations were performed with the ACM in conjunction with the flow solvers FLOWer and TAU. Two different configurations were used. The scaled HIRENASD wing with the structural shell model depicted in Fig. 9 is representative for a real-world transport aircraft wing. The flow conditions were chosen according to a test case defined in the project MEGADESIGN [20] for the optimisation of an aircraft cruise configuration. The flight speed is $Ma = 0.82$ at standard atmospheric conditions in 11 km altitude. These amount to a Reynolds number of $Re = 43.2 \times 10^6$ and a loading factor of $q/E = 0.144 \times 10^{-6}$. This value is the ratio of the free-stream dynamic pressure and Young's modulus of the structure and is a dimensionless number that characterises aeroelastic coupling effects. The second test configuration employed is the HIRENASD wing in its original size and the beam structural model displayed in Fig. 11 representing the structure of the actual wind tunnel model. Results are shown here for the conditions of the experimental polar 250 [4]: $Ma = 0.80$, $Re = 23.5 \times 10^6$ and $q/E = 0.48 \times 10^{-6}$. In both test cases, the dummy fuselage was not taken into consideration. Identical CFD meshes were scaled to match both configurations. The block-structured mesh for FLOWer is the volume mesh from which the already-presented wetted surface with 31245 points was extracted and has about 2.8 million points. The hybrid-unstructured mesh for TAU has 12.6 million points and a wetted surface with 188983 points. Only results obtained with the FIE and MLS methods are compared.

In Fig. 14, the results for the transport aircraft wing configuration are presented. With the MLS method, quadratic interpolation functions were used with $n_{\mathrm{FB}} = 2$ and $N_M = 67$. In the top diagrams, the lift coefficients and the flap-wise bending deflections at the wing tip are plotted over the angle of attack. For both magnitudes the same observation can be made: The projection methods deliver very similar distributions with the same flow solver, but between the results of FLOWer and TAU there is a difference of around 15%. In the bottom left diagram the relative errors in lift and deflection are given. The influence of the projection method is singled out; the deviations between the flow solvers are not shown. The relative error in the tip deflection $|\Delta u_{y,\mathrm{tip}}/u_{y,\mathrm{tip}}|$ is greater than the values obtained in the previous tests (see Fig. 12). During actual coupled simulations the differences between the projection methods affect the structural load distribution as well as the shape of the deformed

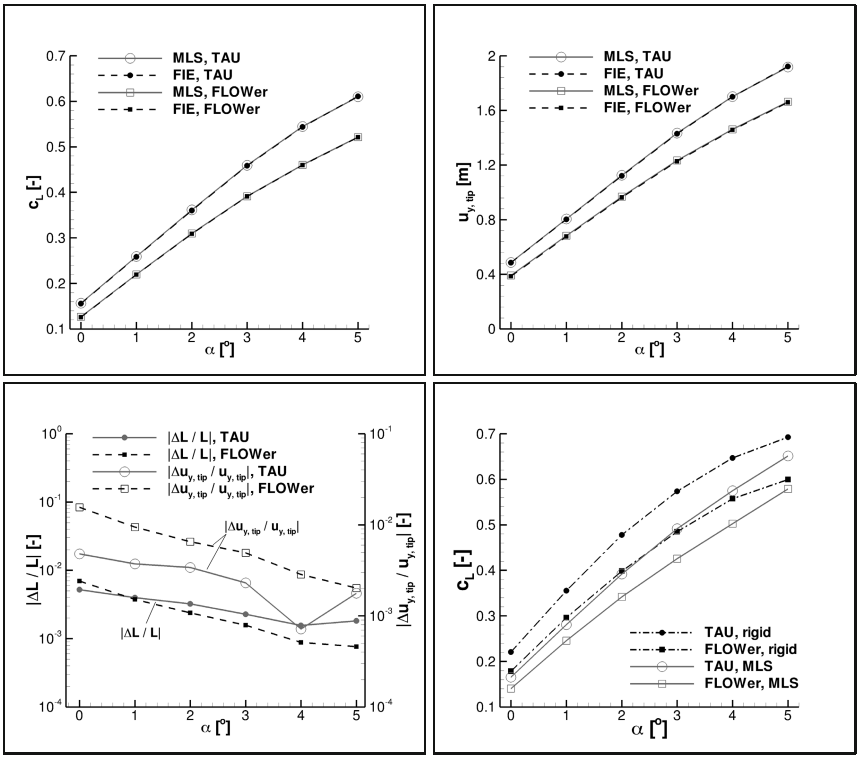

Fig. 14 Results of aeroelastic simulations for the scaled HIRENASD wing and the IFL structural shell model at $Ma = 0.82$, $Re = 43.2 \times 10^6$, $q/E = 0.144 \times 10^{-6}$ and $0° \leq \alpha \leq 5°$. Computations were carried out with FLOWer and TAU coupled with the ACM. FIE and MLS were used as projection methods. In all examples the LEA $k - \omega$ turbulence model and a central differences discretisation in space were applied. *top left:* Lift polars. *top right:* Flapwise tip bending deflections. *bottom left:* Relative errors in lift coefficients and in bending deflections between the projection methods. The comparisons are only carried out between the distributions obtained with the same flow solver. *bottom right:* Lift polars disregarding aeroelastic deformation superimposed on those obtained with MLS. In a departure from the previously shown results, these were obtained with the scaled HIRENASD wing with dummy fuselage.

wetted surface and then feed back to the aerodynamic load distribution of the next coupling iteration. The deviations are still inside engineering limits, though, ranging between one per cent and one per mil. In the bottom right diagram, the lift distributions obtained by "pure" CFD disregarding aeroelastic deformations are additionally provided. Already here the differences are apparent between the flow solvers (These results were obtained for the scaled HIRENASD wing with dummy fuselage, hence the lift coefficients considering aeroelastic deformation are slightly higher than in the top left diagram). In Fig. 15, local pressure distributions at the spanwise

positions $\eta = 0.55$ and $\eta = 0.83$ are picked out for an angle of attack of $\alpha = 3°$. In the undeformed configuration TAU predicts a shock position further downstream than FLOWer by about 5% of the local chord length. The higher structural bending moment must then lead to an aeroelastic equilibrium configuration with larger deformations. The differences between the flow solvers are thus aggravated by the aeroelastic coupling. This test case is entirely generic and there are no experimental data that would allow an evaluation of these differences.

An extensive experimental data base is available for the HIRENASD configuration. Here the same tendencies as with the previous configuration are to be observed, as can be gleaned from Fig. 16. The deformation distributions and the lift polars also coincide well for the projection methods, but there are significant differences between the results of the flow solvers. Measured lift coefficients are superimposed with the simulation results, but do not give a clear direction. Fig. 17 contains calculated and measured pressure distributions for the two highest angles of attack $\alpha = 2°$ and $\alpha = 3°$ at the spanwise stations $\eta = 0.32$, $\eta = 0.59$ and $\eta = 0.80$. The local pressure coefficients by the MLS method and by the FIE method with identical flow solvers coincide excellently, but significant differences between the flow solvers persist. The higher global lift coefficients achieved with TAU are reflected in the higher suction plateaus and shock positions further downstream. For the current test case, predictions with TAU appear in better agreement with the experiments than the FLOWer results, at least at the inboard sections. At $\eta = 0.80$ neither solver correctly captures the gradient at the downstream end of the plateau and its height is overestimated using TAU. Admittedly, the presented simulations do not capture the aerodynamic influence of the dummy fuselage on the flow field about the wing.

The differences between the results of FLOWer and TAU are presumably caused by the flow meshes or the numerical parameters used at CATS, and are not related to

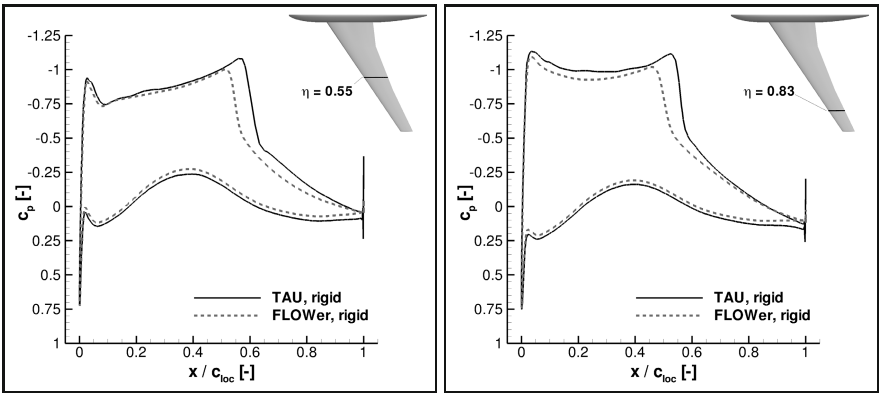

Fig. 15 Pressure distributions obtained with FLOWer and TAU without consideration of aeroelastic deformation at two spanwise stations of the scaled HIRENASD wing with dummy fuselage. Inflow conditions are $Ma = 0.82$, $Re = 43.2 \times 10^6$ and $\alpha = 3°$.

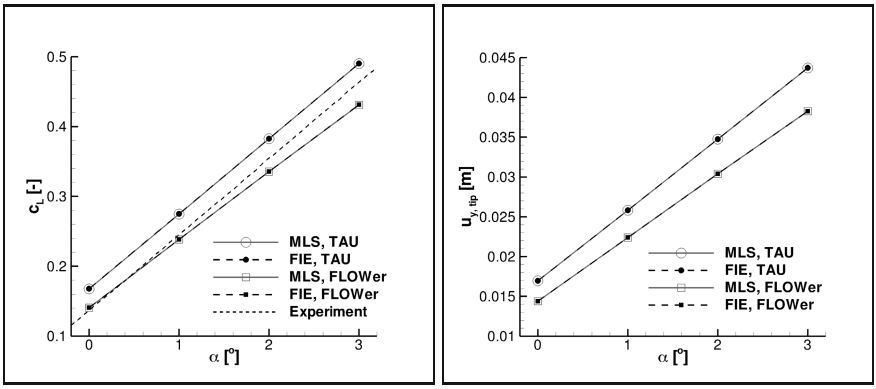

Fig. 16 Results of aeroelastic simulations for the HIRENASD wing with a structural beam model at $Ma = 0.80$, $Re = 23.5 \times 10^6$, $q/E = 0.48 \times 10^{-6}$ and $0° \leq \alpha \leq 3°$. *left:* Lift polars. *right:* Flap-wise tip bending deflections.

the aeroelastic coupling. Further efforts to narrow down the cause of the differences remain to be made, but are outside the scope of the current paper.

6 Conclusion

In this paper, the spatial coupling methods for reduced structural models in the ACM were examined. The existing method for the projection of loads and deformations between the wetted surface and the structure based on FIE was outlined together with the interpolation schemes additionally required for beam models. The alternative methods MLS and GSB and their implementation in the ACM were explained in detail. For the individual steps of the spatial coupling procedure potential error sources were identified. Several test configurations of increasing complexity were used to investigate the importance of the mesh resolutions of the wetted surface and of the structure on the structural load distribution and the resulting deformation field. Only for thin-walled structural models, a significant influence was detected. It manifests itself as local "bumps" on the structure and, after deformation projection, also on the wetted surface. The projection parameters of the FIE, MLS and GSB methods were investigated; their effect on the shape of the deformed wetted surface was determined with two variants of the HIRENASD configuration with and without dummy fuselage and a structural beam model. With the FIE method, only localised effects were apparent in the vicinity of kinks of the beam axis and intersections between assemblies. Here, additional interpolation schemes assure a smooth and contiguous deformed wetted surface. Otherwise, FIE does not rely on interpolation parameters. With MLS and GSB, interpolations are not acting locally, but the projection as a whole is cast as a spatial interpolation problem. (Yet in practice, local interpolations cannot be foregone completely, as without projection results are

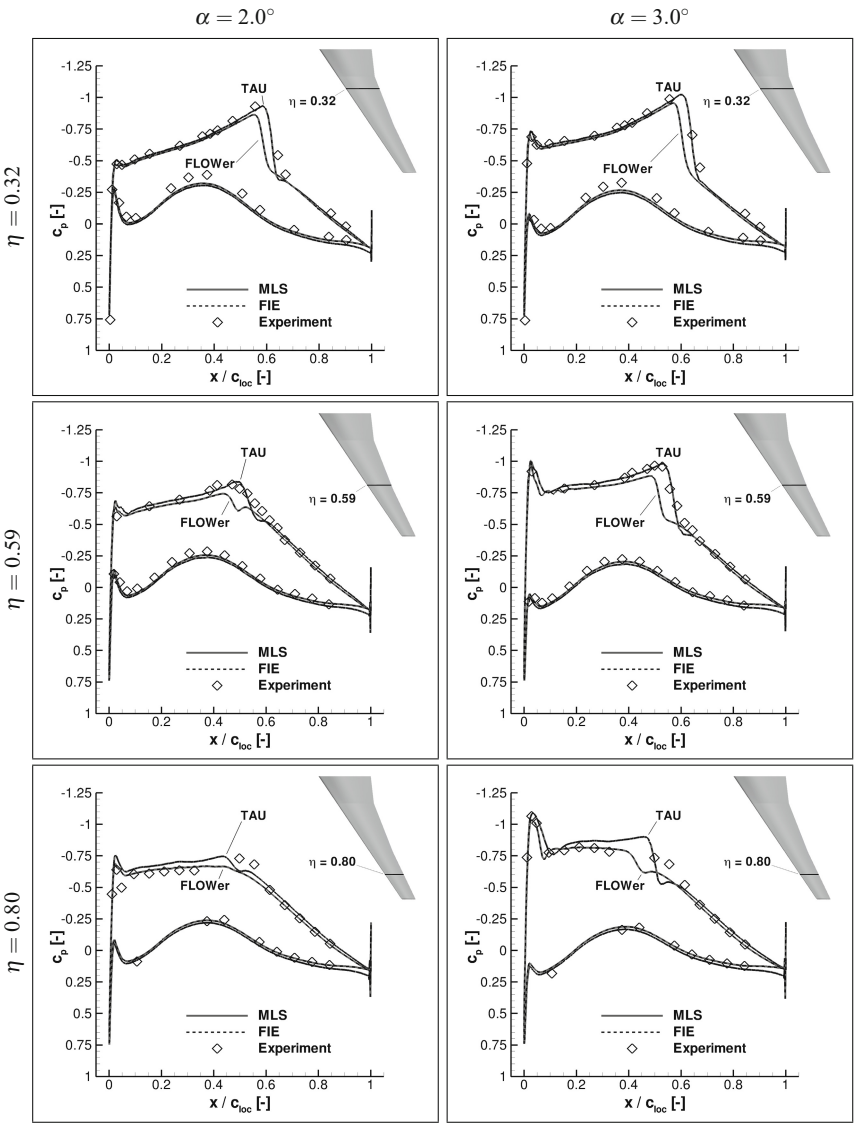

Fig. 17 Measured and computed chordwise pressure distributions for the HIRENASD wing with a structural beam model at $Ma = 0.80$, $Re = 23.5 \times 10^6$ and $q/E = 0.48 \times 10^{-6}$.

unsatisfactory in intersection regions between assemblies.) The MLS method exhibited a low overall dependency on the choice of projection parameters. With the GSB method, the shape of the deformed wetted surface was significantly influenced by the position and number of interpolation support points. By means of coupled simulations with the ACM, and either FLOWer or TAU as flow solvers, the practical

applicability of the MLS method was shown. The differences between the lift polars, deformation distributions and local pressure distributions obtained with MLS and with FIE and identical flow solvers were small. However, in the results achieved with identical projection methods but different flow solvers, significant differences were apparent. These were linked to the flow solvers, respective the input data used, and not to the aeroelastic coupling procedure. Ongoing work on the spatial coupling in the ACM concerns the extension of the FIE method for volume and shell elements to configurations comprising multiple assemblies.

Acknowledgements. Computing resources were provided by the RWTH Aachen University Center for Computing and Communication and supported by the German Research Foundation under GSC 111 (AICES).

References

[1] Ahrem, R., Beckert, A., Wendland, H.: A New Multivariate Interpolation Method for Large-Scale Spatial Coupling Problems in Aeroelasticity. In: Int. Forum Aeroel. Struct. Dyn. (IFASD) 2005, paper IF-073, Munich, Germany (2005)

[2] Badcock, K.J., Rampurawala, A.M., Richards, B.E.: Intergrid Transformation for Aircraft Aeroelastic Simulation. In: 21st Appl. Aerodyn. Conf., AIAA paper 2003-3512, Orlando, USA (2003)

[3] Ballmann, J. (ed.): Flow Modulation and Fluid-Structure Interaction at Airplane Wings—Research Results of the Collaborative Research Center SFB 401 at the RWTH Aachen University, Aachen, Germany. Springer (2003)

[4] Ballmann, J., Boucke, A., Dickopp, C., Reimer, L.: Results of Dynamic Experiments in the HIRENASD Project and Analysis of Observed Unsteady Processes. In: Int. Forum Aeroel. Struct. Dyn. (IFASD) 2009, paper IFASD-2009-103, Seattle, USA (2009)

[5] Beckert, A.: Coupling Fluid (CFD) and structural (FE) Models using Finite Interpolation Elements. Aerosp. Sci. Technol. 4, 13–22 (2000)

[6] Beckert, A., Wendland, H.: Multivariate Interpolation for Fluid-Structure Interaction Problems using Radial Basis Functions. Aerosp. Sci. Technol. 5, 125–134 (2001)

[7] Bendiksen, O.O.: Effect of Wing Deformations and Sweep on Transonic Limit Cycle Flutter of Flexible Wings. In: Int. Forum Aeroel. Struct. Dyn. (IFASD) 2007, paper IF-031, Stockholm, Sweden (2007)

[8] Boucke, A.: Kopplungswerkzeuge für aeroelastische Simulationen. Doctoral thesis, RWTH Aachen University (2003)

[9] Braun, C.: Ein modulares Verfahren für die numerische aeroelastische Analyse von Luftfahrzeugen. Doctoral thesis, RWTH Aachen University (2007)

[10] Cebral, J.R., Löhner, R.: Conservative Load Projection and Tracking for Fluid-Structure Problems. AIAA J. 35(4) (1997)

[11] Chen, P.C., Jadic, I.: Interfacing of Fluid and Structural Models via Innovative Structural Boundary Element Method. AIAA J. 36(2), 282–287 (1998)

[12] Farhat, C., Lesoinne, M., LeTallec, P.: Load and Motion Transfer Algorithms for Fluid/Structure Interaction Problems with Non-Matching Discrete Interfaces: Momentum and Energy Conservation, Optimal Discretization and Application to Aeroelasticity. Comput. Methods Appl. Mech. Eng. 157, 95–114 (1998)

[13] Goura, G.S., Badcock, K.J., Woodgate, M.A., Richards, B.E.: Transformation Methods for the Time Marching Analysis of Flutter. In: 19th AIAA Appl. Aerodyn. Conf., AIAA paper 2001-2457, Anaheim, USA (2001)
[14] Harder, R.L., Desmarais, R.N.: Interpolation Using Surface Splines. J. Aircr. 9, 189–191 (1972)
[15] Heinrich, R., Kroll, N., Neumann, J., Nagel, B.: Fluid-Structure Coupling for Aerodynamic Analysis and Design — A DLR Perspective. In: 46th AIAA Aerosp. Sci. Meet. Exhib., paper AIAA 2008-561, Reno, USA (2008)
[16] Hesse, M.: Entwicklung eines automatischen Gitterdeformationsalgorithmus zur Strömungsberechnung um komplexe Konfigurationen auf Hexaedernetzen. Doctoral thesis, RWTH Aachen University (2006)
[17] Jaiman, R.K., Jiao, X., Geubelle, P.H., Loth, E.: Assessment of Conservative Load Transfer for Fluid-Solid Interface with Non-Matching Meshes. Int. J. Numer. Methods Eng. 55 (2004)
[18] Kroll, N., Rossow, C.-C., Becker, K., Thiele, F.: The MEGAFLOW Project. Aerosp. Sci. Technol. 4(4), 223–237 (2000)
[19] Kroll, N., Fassbender, J.K. (eds.): MEGAFLOW—Numerical Flow Simulation in Aircraft Design. Springer (2005)
[20] Kroll, N. (ed.): MEGADESIGN and MegaOpt—German Initiatives for Aerodynamic Simulation and Optimization in Aircraft Design. Springer (2009)
[21] Massjung, R.: Numerical Schemes and Well-Posedness in Nonlinear Aeroelasticity. Doctoral thesis, RWTH Aachen University (2002)
[22] Park, K.C., Felippa, C.A., Ohayon, R.: Partitioned Formulation of Internal Fluid-Structure Interaction Problems via Localized Lagrange Multipliers. Comput. Methods Appl. Mech. Eng. 190, 2989–3007 (2001)
[23] Quaranta, G., Masarati, P., Mantegazza, P.: A Conservative Mesh-Free Approach for Fluid-Structure Interface Problems. In: Int. Conf. Comp. Methods Coupled Probl. Sci. Eng., Barcelona, Spain (2005)
[24] Reimer, L., Boucke, A., Ballmann, J., Behr, M.: Computational Analysis of High Reynolds Number Aero-Structural Dynamics (HIRENASD) Experiments. In: Int. Forum Aeroel. Struct. Dyn. (IFASD) 2009, paper IFASD-2009-130, Seattle, USA (2009)
[25] Reimer, L., Braun, C., Wellmer, G., Behr, M., Ballmann, J.: Development of a Modular Method for Computational Aero-Structural Analysis of Aircraft. In: Schröder, W. (ed.) Summary of Flow Modulation and Fluid-Structure Interaction Findings—Results of the Collaborative Research Center SFB 401 at the RWTH Aachen University, Aachen, Germany. Springer (1997-2008) (to be published)
[26] van Rossum, G., Drake, F.L.: Using Python Release 3.1.1. Python Software Foundation (2009), `http://www.python.org`
[27] Sadeghi, M., Liu, F., Lai, K.L., Tsai, H.M.: Application of Three-Dimensional Interfaces for Data Transfer in Aeroelastic Computations. In: 22nd Appl. Aerodyn. Conf. Exhib., AIAA paper 2004-5376, Providence, USA (2004)
[28] Schröder, W. (Ed.): Summary of Flow Modulation and Fluid-Structure Interaction Findings — Results of the Collaborative Research Center SFB 401 at the RWTH Aachen University, Aachen, Germany. Springer (1997-2008) (to be published)
[29] Unger, R., Haupt, M.C., Horst, P.: Coupling Techniques for Computational Nonlinear Transient Aeroelasticity. In: 25th Int. Congr. Aeronaut. Sc. (ICAS), paper ICAS 2006-10.2.3, Hamburg, Germany (2006)
[30] Wendland, H.: Piecewise Polynomial, Positive Definite and Compactly Supported Radial Functions of Minimal Degree. Adv. Comput. Math. 4, 389–396 (1995)